

1        The influence of inter-regional delays in generating  
2        large-scale brain networks of phase synchronization

3  
4 Williams N.<sup>1,2</sup>, Ojanperä A.<sup>3</sup>, Siebenhühner F.<sup>4,5</sup>, Toselli B.<sup>6</sup>, Palva S.<sup>4,7</sup>,  
5 Arnulfo G.<sup>4,6</sup>, Kaski S.<sup>1,3,8\*</sup>, Palva J.M.<sup>2,4,7\*</sup>

6  
7 Affiliations:

- 8        1. Helsinki Institute of Information Technology, Department of Computer  
9        Science, Aalto University, Finland
- 10       2. Department of Neuroscience and Biomedical Engineering, Aalto  
11       University, Finland
- 12       3. Department of Computer Science, Aalto University, Finland
- 13       4. Neuroscience Center, Helsinki Institute of Life Science, University of  
14       Helsinki, Finland
- 15       5. BioMag laboratory, HUS Medical Imaging Center, Helsinki, Finland
- 16       6. Department of Informatics, Bioengineering, Robotics & Systems  
17       Engineering, University of Genoa, Italy
- 18       7. Centre for Cognitive Neuroimaging, School of Neuroscience &  
19       Psychology, University of Glasgow, United Kingdom
- 20       8. Department of Computer Science, University of Manchester, United  
21       Kingdom

22  
23  
24  
25

26 \* Equally contributing authors

27

28 Corresponding author:

29 Dr. Nitin Williams

30 Helsinki Institute of Information Technology (HIIT)

31 Department of Computer Science, Aalto University

32 Konemiehentie 2, 02150

33 Espoo, Finland

34 Email: [nitin.williams@aalto.fi](mailto:nitin.williams@aalto.fi)

## 35 Highlights

- 36 ● Compared methods to specify delays in Biophysical Network Models (BNMs)
- 37 ● BNM with “distance-dependent” conduction delays more probable than alternatives
- 38 ● BNMs with biologically informed prior distributions generate dynamics seen in MEG
- 39 ● Fitting BNMs yields reliable posterior distributions informed by MEG data ( $N = 75$ )

40

41

42

43

44

45

46

47

48

49

50

51

## 52 Abstract

53 Large-scale networks of phase synchronization are considered to regulate the communication  
54 between brain regions fundamental to cognitive function, but the mapping to their structural  
55 substrates, *i.e.*, the structure-function relationship, remains poorly understood. Biophysical  
56 Network Models (BNMs) have demonstrated the influences of local oscillatory activity and  
57 inter-regional anatomical connections in generating alpha-band (8–12 Hz) networks of phase  
58 synchronization observed with Electroencephalography (EEG) and Magnetoencephalography  
59 (MEG). Yet, the influence of inter-regional conduction delays remains unknown. In this study,  
60 we compared a BNM with standard “distance-dependent delays”, which assumes constant  
61 conduction velocity, to BNMs with delays specified by two alternative methods accounting for  
62 spatially varying conduction velocities, “isochronous delays” and “mixed delays”. We  
63 followed the Approximate Bayesian Computation (ABC) workflow, i) specifying  
64 neurophysiologically informed prior distributions of BNM parameters, ii) verifying the  
65 suitability of the prior distributions with Prior Predictive Checks, iii) fitting each of the three  
66 BNMs to alpha-band MEG resting-state data ( $N = 75$ ) with Bayesian Optimisation for  
67 Likelihood-Free Inference (BOLFI), and iv) choosing between the fitted BNMs with ABC  
68 model comparison on a separate MEG dataset ( $N = 30$ ). Prior Predictive Checks revealed the  
69 range of dynamics generated by each of the BNMs to encompass those seen in the MEG data,  
70 suggesting the suitability of the prior distributions. Fitting the models to MEG data yielded  
71 reliable posterior distributions of the parameters of each of the BNMs. Finally, model  
72 comparison revealed the BNM with “distance-dependent delays”, as the most probable to  
73 describe the generation of alpha-band networks of phase synchronization seen in MEG. These  
74 findings suggest that distance-dependent delays contribute significantly to the neocortical  
75 architecture of human alpha-band networks of phase synchronization. Hence, our study  
76 illuminates the role of inter-regional delays in generating the large-scale networks of phase  
77 synchronization that might subserve the communication between regions vital to cognition.

78

79 **Keywords:** Biophysical Network Models (BNMs); Magnetoencephalography (MEG) resting-  
80 state; Axonal conduction delays; Phase synchronization; Approximate Bayesian Computation  
81 (ABC); Bayesian Optimisation for Likelihood-Free Inference (BOLFI)

## 82 1. Introduction

83 Communication between brain regions is fundamental to all sensorimotor and cognitive  
84 functions (Fries (2015), Buszáki (2006), Varela et al. (2001)). Phase synchronization between  
85 neuronal oscillations from different brain regions is considered to subserv inter-regional  
86 communication by regulating the relation of spike arrival times to windows of excitability in  
87 the receiving brain region (Fries (2015), Fries (2005), Womelsdorf et al. (2007), Salazar et al.  
88 (2012)). Distinct sets of brain regions are recruited into networks of phase synchronization in  
89 tasks involving, *e.g.*, working memory (Kitzbichler et al. (2011), Palva et al. (2010)), language  
90 (Doesburg et al. (2016)), visual attention (Lobier et al. (2018), Gross et al. (2004)), and  
91 sensorimotor processing (Hirvonen et al. (2018)). Neurophysiological studies have revealed  
92 reciprocal interactions between excitatory and inhibitory neuronal populations to underlie  
93 intra-regional phase synchronization (Buzsáki (2006), Traub (1997), Gray (1994)). However,  
94 the mapping between large-scale, inter-regional networks of phase synchronization and their  
95 structural substrates, *i.e.*, the structure-function relationship, remains poorly understood.

96  
97 Biophysical Network Models (BNMs) comprise models of individual brain regions linked by  
98 biologically informed patterns of anatomical connections via finite conduction delays  
99 (Woolrich & Stephan (2005)). BNMs are a powerful tool to understand the structure-function  
100 relationship pertaining to inter-regional networks of phase synchronization (Breakspear  
101 (2017)). BNMs have been used to demonstrate the influences of oscillatory activity from  
102 neuronal populations (Forrester et al. (2020)), the pattern of inter-regional anatomical  
103 connections (Finger & Bönstrup et al. (2016)), and inhibitory synaptic plasticity (Abey Suriya  
104 et al. (2018)), in generating large-scale networks of phase synchronization observed in  
105 Electroencephalography (EEG) or Magnetoencephalography (MEG) resting-state. They have  
106 also been used to relate the heterogeneity of inter-regional conduction delays to the observed  
107 (Dotson et al. (2014)) bimodal distribution in angles of inter-regional phase synchronization  
108 (Petkoski et al. (2018), Petkoski & Jirsa (2019)). However, the influence of inter-regional  
109 delays in generating the pattern of connection strengths in large-scale networks of phase  
110 synchronization observed in EEG or MEG resting-state, has not been investigated.

111

112 BNMs typically specify inter-regional delays by dividing the Euclidean distance between  
113 regions with a biologically-informed but spatially uniform conduction velocity (Abey Suriya et  
114 al. (2018), Hadida et al. (2018), Cabral et al. (2014), Nakagawa et al. (2014), Deco et al. (2009),

115 Ghosh et al. (2008)). BNMs with “distance-dependent delays” assuming spatially uniform  
116 conduction velocity have been used to generate alpha-band (8–12 Hz) inter-regional networks  
117 of phase synchronization corresponding to those observed in MEG (Abey Suriya et al. (2018))  
118 and EEG resting-state (Finger & Bönstrup et al. (2016)). However, a wealth of evidence from  
119 human intra-cranial EEG recordings (Trebaul et al. (2018), Lemaréchal et al. (2022)) and  
120 animal electrophysiological studies across species (Chomiak et al. (2008), Swadlow et al.  
121 (1978), Miller (1975), Swadlow (1990), Simmons & Pearlman (1983)) report spatially varying  
122 conduction velocities. Theoretical proposals have suggested that the fine temporal co-  
123 ordination in many cognitive functions requires regulating conduction velocities, to  
124 compensate for delay heterogeneity due to varying connection lengths (Seidl (2014), Pajevic  
125 et al. (2014)). Myelination of neurons can regulate conduction velocities through the linear  
126 relationship between outer axonal diameter and conduction velocity (Rushton (1951), Waxman  
127 & Bennett (1972)). Computational models incorporating activity-dependent myelination have  
128 been demonstrated to yield inter-regional connections with highly similar conduction delays,  
129 irrespective of the length of these connections (Noori et al. (2020)). Animal  
130 electrophysiological studies (Salami et al. (2003), Carr & Konishi (1990)) have also found  
131 evidence for “isochronous delays”, *i.e.*, highly similar delays, across connections, possibly as  
132 a result of activity-dependent myelination. Alternative theoretical proposals have suggested  
133 that the need for fine temporal co-ordination might be balanced by the high metabolic costs of  
134 myelinating long-distance connections (Aboitiz et al. (2003)), resulting in a combination of  
135 “distance-dependent” and “isochronous” inter-regional conduction delays. In line with this  
136 proposal, animal electrophysiological studies have found evidence for isochronous delays in  
137 ipsilateral but not contralateral connections (Chomiak et al. (2008)). However, these  
138 alternative, biologically plausible methods to specifying inter-regional delays in BNMs, have  
139 not been compared to the standard “distance-dependent delays” method.

140

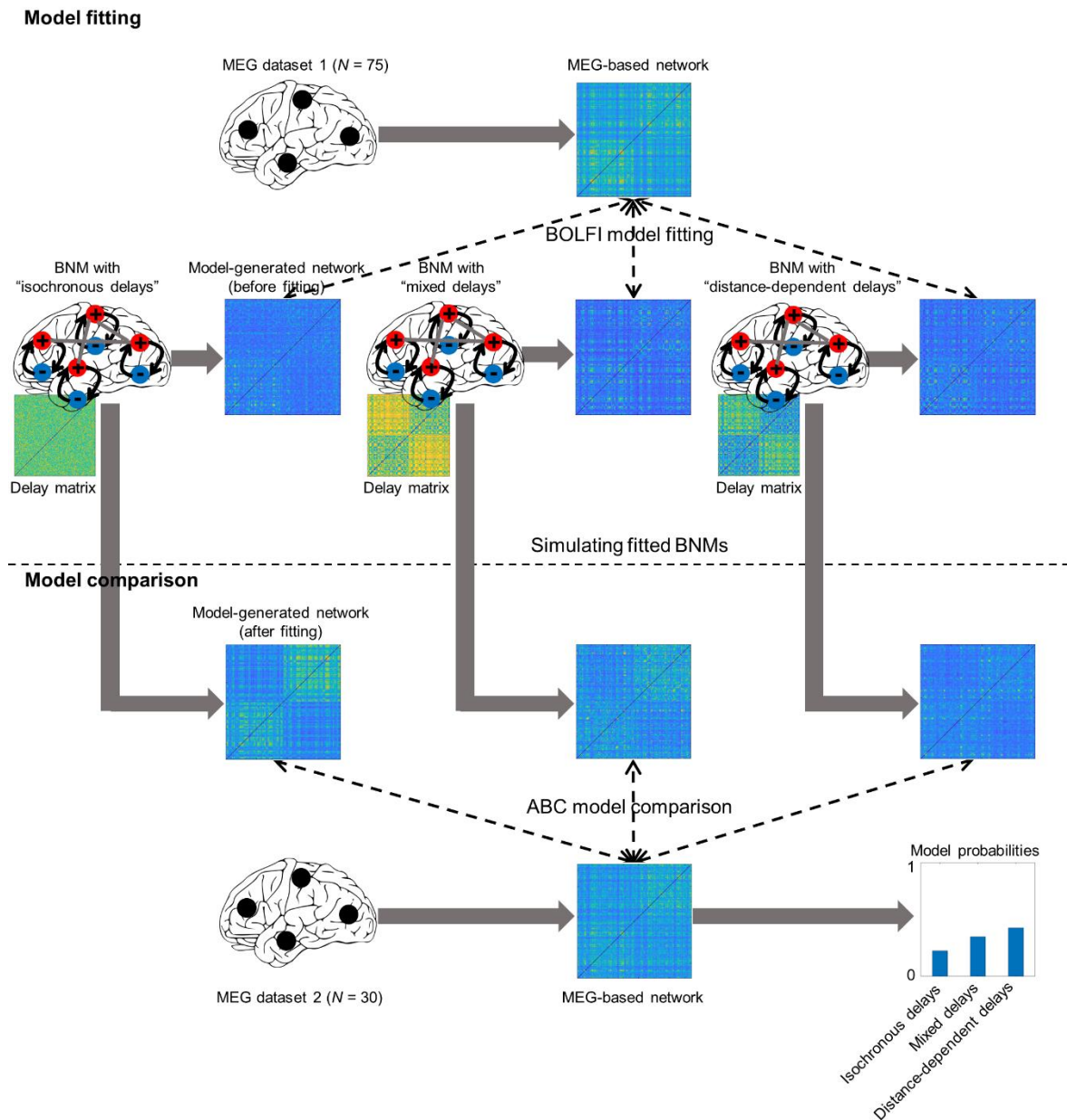
141 In this study, we compared the “distance-dependent delays” method to two alternative  
142 biologically plausible methods to specifying inter-regional delays in BNMs of alpha-band (8–  
143 12 Hz) networks of phase synchronization. We focused on alpha-band frequencies i) because  
144 they provide a basis to compare against previously proposed BNMs of phase synchronization  
145 (Abey Suriya et al. (2018), Finger & Bönstrup et al. (2016)), which also focused on alpha-band  
146 frequencies, ii) because of the clear evidence for alpha-band oscillations manifested as a  
147 spectral peak in the 8–12 Hz range both in our own MEG dataset (see Section 2.1) and in  
148 previous human electrophysiological studies (Mahjoory et al. (2020), Donoghue et al. (2020),

149 Wang (2010)) - oscillations are a pre-requisite for phase synchronization, and iii) because of  
150 the prominent functional role of alpha-band oscillations in cognitive functions, *e.g.*, stimulus  
151 suppression, stimulus selection and top-down modulation (Palva & Palva (2007), Foxe &  
152 Snyder (2011), Klimesch (2012)). Apart from a standard BNM with “distance-dependent  
153 delays”, we defined a BNM with “isochronous delays” which assumed highly similar inter-  
154 regional delays across connections, and a BNM with “mixed delays” which assumed inter-  
155 regional delays to be a function of both the distance between regions and an isochronous or  
156 constant delay.

157

158 We followed an Approximate Bayesian Computation (ABC) workflow to compare the three  
159 BNMs. To do this, we first specified prior distributions for parameters of each of the three  
160 BNMs based on strong neurophysiological constraints derived from the aggregated animal  
161 electrophysiology literature (Tripathy et al. (2014), Tripathy et al. (2015)). In these models,  
162 prior distributions are probability distributions reflecting our existing knowledge on the values  
163 of BNM parameters, while posterior distributions are probability distributions reflecting our  
164 updated knowledge on the values of BNM parameters after accounting for evidence from MEG  
165 data. We ran Prior Predictive Checks to verify the suitability of the chosen prior distributions,  
166 and then applied Bayesian Optimisation for Likelihood Free Inference (BOLFI) (Gutmann &  
167 Corander (2016)) to separately fit the BNMs with “distance-dependent delays”, “isochronous  
168 delays”, and “mixed delays”, to an experimental MEG resting-state dataset ( $N = 75$ ). Finally,  
169 we used ABC model comparison (Beaumont (2019)) to compare the three fitted BNMs with  
170 an independent MEG resting-state dataset ( $N = 30$ ). The Prior Predictive Checks revealed the  
171 range of dynamics generated by the three BNMs to encompass those reflected by the phase  
172 synchronization phenomena we observed in MEG resting-state. This suggested the suitability  
173 of the prior distributions of the parameters of all three BNMs. Fitting the three BNMs to  
174 experimental MEG data with BOLFI yielded reliable posterior distributions, representing  
175 constraints on the values of BNM parameters after accounting for evidence from the MEG data.  
176 Finally, ABC model comparison revealed the BNM with “distance-dependent delays” as more  
177 probable than the other BNMs, to describe the mechanisms generating large-scale alpha-band  
178 networks of phase synchronization observed in MEG resting-state.

## 179 2. Materials & Methods



180

181 **Figure 1. Workflow comparing strategies to specify inter-regional delays in Biophysical**  
182 **Network Models (BNMs) of phase synchronization.** Bayesian Optimisation for Likelihood-  
183 Free Inference (BOLFI) was used to fit BNMs with “isochronous delays”, “mixed delays”,  
184 and “distance-dependent delays” to Magnetoencephalographic (MEG) resting-state data ( $N =$   
185  $75$ ), *i.e.* to determine parameter values for each of the three BNMs that would generate alpha-  
186 band inter-regional networks of phase synchronization corresponding closely to those  
187 observed in MEG resting-state. Approximate Bayesian Computation (ABC) model  
188 comparison was then used to choose between BNMs with “isochronous delays”, “mixed

189 delays”, and “distance-dependent delays”, by comparing their alpha-band networks of phase  
190 synchronization to those observed in an independent MEG dataset ( $N = 30$ ).

191

192 We used an ABC workflow to compare the “isochronous delays”, “mixed delays”, and  
193 “distance-dependent delays” methods of specifying inter-regional delays in BNMs of alpha-  
194 band networks of phase synchronization (Figure 1). First, we employed the high-dimensional  
195 ABC inference method BOLFI (Gutmann & Corander (2016)) to fit BNMs with “isochronous  
196 delays”, “mixed delays”, and “distance-dependent delays”, to an MEG resting-state dataset  
197 ( $N = 75$ ). Then, we used ABC model comparison (Beaumont (2019)) to choose between the  
198 three fitted BNMs on an independent MEG resting-state dataset ( $N = 30$ ). We used the ABC  
199 workflow since it provides methods to fit and compare BNMs despite their likelihood  
200 functions being intractable or mathematically difficult to formulate (Green et al. (2015),  
201 Lintusaari et al. (2017)). Further, ABC methods perform Bayesian inference (Gelman et al.  
202 (2013), van de Schoot et al. (2021), Gelman et al. (2020)), which provides a principled  
203 framework i) to combine existing knowledge from *e.g.*, animal electrophysiology with  
204 evidence from observed MEG data to estimate values of BNM parameters, and ii) to account  
205 for uncertainty in the values of BNM parameters. We express existing knowledge of BNM  
206 parameters as prior distributions while we express updated knowledge of BNM parameters,  
207 given the observed data, as posterior distributions. Marginal distributions represent the  
208 probability distributions of individual BNM parameters irrespective of the values of other  
209 BNM parameters. Conditional distributions represent the probability distributions of  
210 individual BNM parameters given the value of another BNM parameter. Joint distributions  
211 represent the probability distribution of all BNM parameters given the values of all other  
212 BNM parameters. In this paper, we refer to marginal prior and posterior distributions of BNM  
213 parameters as simply their “prior distributions” and “posterior distributions” respectively,  
214 while we refer to conditional or joint prior and posterior distributions by their entire names,  
215 *e.g.*, “conditional prior distribution”.

## 216 2.1 BNM specification

217 BNMs comprise models of individual brain regions linked by biologically informed patterns  
218 of anatomical connections with finite conduction delays. For BNMs implementing each of  
219 the delay specification methods, we used Wilson-Cowan (WC) oscillators to model the  
220 dynamics of individual brain regions (Wilson & Cowan (1972), Kilpatrick (2013), Cowan et



221 al. (2016)). WC oscillators have been used to model dynamics of individual brain regions in a  
222 number of modelling studies emulating brain functional networks (Hadida et al. (2018),  
223 Hellyer et al. (2016), Heitmann et al. (2017)), including modelling studies on inter-regional  
224 networks of phase synchronization (Abey Suriya et al. (2018), Hlinka & Coombes (2012)).  
225 The dynamics of WC oscillators arise from the interaction between excitatory and inhibitory  
226 neuronal populations, *i.e.*, the Pyramidal Inter-Neuronal Gamma (PING) model of oscillation  
227 generation (Traub et al. (1997)) and are also influenced by external inputs and the dynamics  
228 of linked oscillators. Hence, the ensemble of connected WC oscillators represented our  
229 current understanding on the generation of neuronal oscillations and inter-regional phase  
230 synchronization (Buzsáki (2006), Gray (1994)). The dynamics of oscillator  $x$  is given by:

231

$$232 \quad \tau_e \frac{dU_e}{dt} = -U_e(t) + F(w_{ee}U_e(t) - w_{ei}U_i(t) - b_e + J_e + \psi_e(t) + k \sum_{y=1}^N IH(x, y) \cdot K(x, y) U_e(t - T(x, y)))$$

$$233 \quad \tau_i \frac{dU_i}{dt} = -U_i(t) + F(w_{ie}U_e(t) - w_{ii}U_i(t) - b_i + J_i + \psi_i(t)) \quad (1)$$

234

235 where  $T$  is an  $N \times N$  matrix, with  $T(x, y)$  specifying the inter-regional conduction delay from  
236 brain region  $y$  to brain region  $x$ , in milliseconds.  $N$  is the number of brain regions or WC  
237 oscillators. We assumed the dynamics of each of the  $N$  brain regions to be governed by equation  
238 1, in line with the assumption of identical brain regions in previous modelling studies of inter-  
239 regional phase synchronization in MEG (Abey Suriya et al. (2018), Finger & Bönstrup et al.  
240 (2016)). Further, we assumed all  $N$  brain regions to generate oscillatory dynamics, in agreement  
241 with the previously reported cortex-wide alpha-band spectral peaks in a large MEG resting-  
242 state dataset ( $N = 187$ ) (Mahjoory et al. (2020)) as well as the prominent alpha-band spectral  
243 peak across regions and subjects in our own MEG dataset ( $N = 75$ ) (Figure S1) – spectral peaks  
244 are a signature of oscillatory dynamics (Wang (2010)).

245

246 For the BNM with “distance-dependent delays”, we estimated  $T(x, y)$  by dividing the Euclidean  
247 distance between regions  $x$  and  $y$  (in mm) by a scalar value  $v$ , which was the spatially uniform  
248 conduction velocity (in metres/second) assumed by distance-dependent delays. We estimated  
249 Euclidean distance between the centroids of brain regions in MNI space. For the BNM with  
250 “isochronous delays”, we populated the upper triangular elements of  $T$  by sampling from a  
251 Gaussian distribution whose mean was given by a *delay* parameter (in milliseconds) and whose  
252 standard deviation was given by the product of the *delay* parameter and a *coeffvar<sub>delay</sub>*

253 parameter, which controlled the coefficient of variation around the mean. We constrained each  
254 of the delays to be positive using the ‘absolute’ operation and then constrained each of the  
255 delays to be integers using the ‘ceiling’ operation. Finally, we constrained the delays to be  
256 identical in both directions, *i.e.*,  $T(x,y)=T(y,x)$  for all  $x$  and  $y$  values, by copying all upper-  
257 triangular elements of  $T(x,y)$  to their corresponding lower-triangular elements. For the BNM  
258 with “mixed delays”, the inter-regional delays were determined both by an inter-regional  
259 distance term as well as a constant or isochronous delay term. We implemented the “mixed  
260 delays” method by first estimating the  $N \times N$  velocity matrix  $V_{distance}$  implied by the distance-  
261 dependent contribution. To do this, we set all non-diagonal elements of  $V_{distance}$  to the value of  
262 the spatially uniform conduction velocity  $v$  assumed by distance-dependent delays. We next  
263 estimated the velocity matrix  $V_{isochronous}$  implied by the isochronous delay contribution. To do  
264 this, we divided the  $N \times N$  matrix of inter-regional distances by the scalar value of *delay*  
265 parameter assumed by isochronous delays. We then combined the  $V_{distance}$  and  $V_{isochronous}$   
266 matrices in the relative proportion specified by the *coefbalance* parameter, which typically  
267 assumed values between 0 and 1. We estimated the  $N \times N$  velocity matrix  $V_{mixed}$  implied by  
268 “mixed delays” by:

$$269 \quad V_{mixed}(x,y) = coefbalance(V_{distance}(x,y)) + (1 - coefbalance)(V_{isochronous}(x,y)) \quad (2)$$

271  
272 Finally, we estimated the  $N \times N$  matrix  $T$  of “mixed delays” by an element-wise division of  
273 the  $N \times N$  matrices of inter-regional distances and the  $N \times N$  velocity matrix,  $V_{mixed}$ . We  
274 constrained all delays to be positive using the ‘ceiling’ operation. Please refer Figure S2 for  
275 illustrations of example matrices of conduction velocities and resulting matrices of inter-  
276 regional delays for the “isochronous delays”, “mixed delays” and “distance-dependent  
277 delays” methods.  $F(z) = \frac{1}{1+e^{-z}}$  is a sigmoid function,  $U_e(t)$  and  $U_i(t)$  are the mean firing rates at  
278 time  $t$  of the excitatory and inhibitory populations respectively,  $w_{ee}$  and  $w_{ii}$  are the excitatory-  
279 excitatory and inhibitory-inhibitory connection weights respectively,  $w_{ie}$  and  $w_{ei}$  are the  
280 excitatory-inhibitory and inhibitory-excitatory connection weights,  $b_e$  and  $b_i$  correspond to the  
281 firing thresholds of excitatory and inhibitory populations,  $J_e$  and  $J_i$  are injection currents to  
282 excitatory and inhibitory populations,  $\psi_e(t)$  and  $\psi_i(t)$  are noise input modelled by a Gaussian  
283 process with zero mean and standard deviation given by  $\psi_{sigma}$ ,  $\tau_e$  and  $\tau_i$  are the time  
284 constants of the excitatory and inhibitory populations, and  $k$  is a scalar multiplier over the  
285 coupling matrix  $K$ , which is an  $N \times N$  matrix.  $K(x,y)$  is the strength of the structural  
286 connection from brain region  $y$  to brain region  $x$ .  $IH$  is an  $N \times N$  matrix that we used to

287 selectively scale inter-hemispheric structural connections to compensate for the known under-  
288 estimation of long-distance connections by diffusion MRI-based tractography (Sotiropoulos  
289 & Zalesky (2019)). We specified the  $IH$  matrix by setting all elements corresponding to intra-  
290 hemispheric connections to 0, while we set all elements corresponding to inter-hemispheric  
291 connections to an identical positive value given by the  $IH_{scaling}$  parameter.

292

293 Each of the three BNMs had 11 parameters in common, *i.e.*, those parameters corresponding  
294 to the dynamics of individual brain regions and the structural connectome. In addition, the three  
295 BNMs had different sets of parameters to specify the matrix of inter-regional delays - the BNM  
296 with “distance-dependent delays” had the  $v$  parameter, the BNM with “isochronous delays”  
297 had the  $delay$  and  $coeffvar_{delay}$  parameters, while the BNM with “mixed delays” had the  $v$ ,  
298  $delay$  and  $coeff_{balance}$  parameters.

### 299 2.1.1 Specifying strength of structural connections between WC oscillators

300 We specified the number and positions of brain regions as per the Destrieux brain parcellation  
301 (Destrieux et al. (2010)), whose 148 regions provided a balance between biologically detailed  
302 brain regions and computationally tractable model simulations. We specified the strengths of  
303 structural connections between WC oscillators by first estimating a  $148 \times 148$  Destrieux atlas-  
304 based group-averaged ( $N = 57$ ) matrix of the number of streamlines between brain regions,  
305 estimated by constrained spherical deconvolution (Smith et al. (2013)) and probabilistic  
306 tractography (Smith et al. (2012)) on pre-processed DWI images from the Human Connectome  
307 Project (van Essen et al. (2013)). The strengths of structural connections varied across seven  
308 orders of magnitude, *i.e.*, from  $10^{-2}$  through  $10^4$ , and log-transformed strengths were inversely  
309 related to Euclidean distance between brain regions (Figure S3). We normalised each element  
310 in the structural connectivity matrix by its row-sum (Hlinka & Coombes (2012), Forrester  
311 (2020)). This normalisation strategy adjusts for potential tractography-induced confounds  
312 between streamline counts and sizes of brain regions. Similar strategies have been shown to  
313 improve the correspondence between diffusion MRI tractography-based structural connectivity  
314 estimates and those from retrograde tracer injections in macaque (Donahue et al. (2016)).

### 315 2.1.2 Simulating the model

316 We simulated all three BNMs with the DDE23a integrator (Shampine & Thompson (2001)),  
317 through the Brain Dynamics Toolbox (BDT) (Heitmann et al. (2018)). We ran the model

318 simulations for 65 seconds with a 250 Hz sampling frequency, and set Absolute Tolerance to  
319  $1 \times 10^{-6}$  and Relative Tolerance to  $1 \times 10^{-3}$ , to limit local discretisation error. We discarded  
320 data from the first 5 seconds to minimise the effect of transient dynamics. We used dynamics  
321 of only the excitatory neuronal populations for further processing since the pyramidal neurons  
322 in excitatory populations are the dominant contributors to the measured MEG signals (Lopes  
323 da Silva (2013)). The dynamics of the excitatory neuronal populations represented the mean  
324 firing rate of pyramidal neurons in these populations.

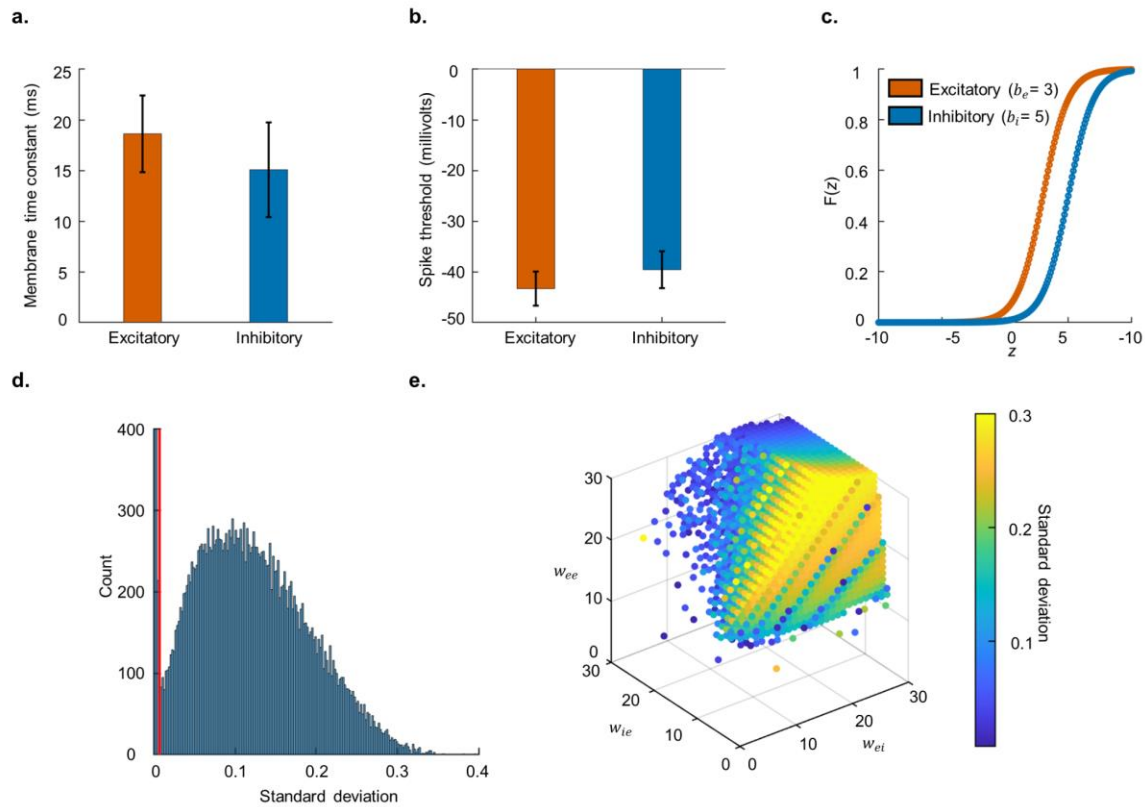
## 325 2.2 Prior specification

326 We specified prior distributions of BNM parameters as Gaussian distributions whose mean  
327 and standard deviation we set based on i) biological constraints, including values reported in  
328 the aggregated animal electrophysiology literature and human intra-cranial EEG recordings,  
329 ii) values found to be optimal in the MEG and functional Magnetic Resonance Imaging  
330 (fMRI) modelling literature on brain functional networks, and iii) ranges of values generating  
331 oscillatory dynamics - oscillations are a pre-requisite of phase synchronization.

332

### 333 *Prior distributions of $\tau_e$ and $\tau_i$*

334 We set the prior distribution of  $\tau_e$ , the time constant of excitatory neuronal populations, to  
335  $18.6 \pm 3.6$  ms (mean  $\pm$  standard deviation) (Figure 2a) based on the weighted mean and  
336 pooled standard deviation of ‘layer 2/3 pyramidal neurons’ time constants in the  
337 NeuroElectro database (Tripathy et al. (2015)). We used values from ‘layer 2/3 pyramidal  
338 neurons’ since post-synaptic potentials (PSPs) from apical dendrites of supra-granular  
339 neurons are the dominant contributors to the measured MEG signal (Baillet (2017)). We set  
340 the prior distribution of  $\tau_i$ , the time constant of inhibitory neuronal populations, to  $15.1 \pm 4.7$   
341 ms based on the weighted mean and pooled standard deviation of time constants of different  
342 cortical inhibitory cell types in the NeuroElectro database: ‘basket cells’, ‘double bouquet  
343 cells’, ‘chandelier cells’, ‘Martinotti cells’, ‘bipolar cells’ and ‘interneurons from deep  
344 cortical layers’. We used values from diverse inhibitory cell types due to the variety of  
345 inhibitory cell types forming connections to ‘layer 2/3 pyramidal neurons’ (Markram et al.  
346 (2004)). We fixed  $J_e$  and  $J_i$ , injection currents to excitatory and inhibitory populations to 0,  
347 reflecting negligible sensory and thalamic input at resting-state (Meijas et al. (2016)).



348

349 **Figure 2. Prior specification** **a.** Bar plot for time constants of excitatory and inhibitory  
 350 neurons across multiple studies reported in NeuroElectro database. Whiskers indicate  
 351 standard deviation. **b.** Bar plot for spike thresholds of excitatory and inhibitory neurons  
 352 across multiple studies reported in NeuroElectro database. **c.** Logistic function curves for  
 353  $b_e=3$  and  $b_i=5$ , where  $b_e$  and  $b_i$  are firing thresholds of the excitatory and inhibitory neuronal  
 354 populations respectively. **d.** Histogram for standard deviation of activity from excitatory  
 355 neuronal populations across multiple combinations of plausible parameter values for  $w_{ee}$ ,  $w_{ei}$ ,  
 356  $w_{ie}$  and  $w_{ii}$ , which are connection strengths within and between excitatory and inhibitory  
 357 neuronal populations. Vertical red line indicates standard deviation threshold of  $7 \times 10^{-3}$ , to  
 358 detect oscillatory dynamics. **e.** 3-D scatter plot displaying combinations of  $w_{ee}$ ,  $w_{ei}$  and  $w_{ie}$ ,  
 359 generating oscillatory dynamics. Colour of dots indicates standard deviation of dynamics.

360

### 361 *Prior distributions of $b_e$ and $b_i$*

362 We set the prior distribution of  $b_e$ , the firing threshold of excitatory neuronal populations, to 3  
 363  $\pm 1$ . We set the mean to a positive value since neurons fire in response to net excitation. We  
 364 used a low value since the typical excitation of 20 millivolts (from -60 millivolts resting-state  
 365 to -40 millivolts spike threshold) at which neurons fire, is small compared to the 100 millivolt  
 366 range of the membrane potential (Kandel & Schwartz (1985)). We set the prior distribution of

367  $b_i$ , the firing threshold of inhibitory neuronal populations, to  $5 \pm 1$ . We set the mean to 5 due  
368 to the higher spike thresholds of inhibitory neurons (-39.6 millivolts) compared to excitatory  
369 neurons (-43.2 millivolts) (Figure 2b), as per values in the NeuroElectro database (Tripathy et  
370 al. (2015)). Higher spike thresholds of inhibitory neurons is also in agreement with the high  
371 spike thresholds of nest basket cells, which make up a high proportion of inhibitory neurons  
372 (Wang et al. (2002)). We set the standard deviation to 1, to reflect the partial overlap in the  
373 spike thresholds of excitatory and inhibitory neurons (Figure 2b). Prior means of  $b_e$  and  $b_i$  set  
374 firing thresholds of excitatory and inhibitory populations to 3 and 5 respectively (Figure 2c).

375

#### 376 *Prior distributions of $w_{ee}$ , $w_{ei}$ , $w_{ie}$ and $w_{ii}$*

377 We set the prior distribution of  $w_{ii}$ , strength of connections within inhibitory neuronal  
378 populations, to  $1 \pm 0.2$ . These values reflected the strict biological constraint of sparse  
379 recurrent structural connectivity between inhibitory interneurons (Markram et al. (2004),  
380 Binzegger et al. (2004)). We set the prior distributions of  $w_{ee}$ ,  $w_{ei}$  and  $w_{ie}$ , connection  
381 strengths within excitatory neuronal populations, from inhibitory to excitatory, and excitatory  
382 to inhibitory, to  $20 \pm 5$ ,  $18 \pm 6$  and  $18 \pm 6$  respectively. These reflected ranges of parameters  
383 values generating oscillatory dynamics, as defined by a standard deviation threshold (Figure  
384 2d–e). The higher value of the prior mean for  $w_{ee}$  compared to those of  $w_{ei}$  and  $w_{ie}$  reflected  
385 the biological constraint of dense structural connections between ‘layer 2/3 pyramidal  
386 neurons’ (Binzegger et al. (2004), Douglas et al. (1989), Douglas & Martin (2007), Jansen &  
387 Rit (1995)). The wide standard deviations for  $w_{ee}$ ,  $w_{ei}$  and  $w_{ie}$  reflected the uncertainty in their  
388 values due to differing reports on their relative magnitudes - anatomical studies report  
389 structural connections within excitatory populations to be much denser than those between  
390 excitatory and inhibitory populations (Binzegger et al. (2004), Douglas & Martin (2007)),  
391 while physiological studies report functional connections within excitatory populations to  
392 have similar strength to functional connections between excitatory and inhibitory populations  
393 (Seeman & Campagnola et al. (2018), Campagnola & Seeman et al. (2022)).

394

#### 395 *Prior distributions of $\psi_{sigma}$ , $k$ , and $IH_{scaling}$*

396 We set the prior distribution of  $\psi_{sigma}$ , *i.e.*, standard deviation of the noise input to excitatory  
397 and inhibitory populations, to  $0.15 \pm 0.05$ . The very low values assumed by  $\psi_{sigma}$  respected  
398 the biological constraint of negligibly small probability that a neuronal population fires solely  
399 due to noise input (Faisal et al. (2008)). Further, these settings allowed  $\psi_{sigma}$  to encompass

400 values between 0.01 and 0.32 found to be optimal in previous MEG and fMRI modelling  
401 studies (Abey Suriya et al. (2018), Hellyer et al. (2016), Deco et al. (2009)). We set the prior  
402 distribution of  $k$ , the scalar multiplier over the structural connectome, to  $1.5 \pm 0.5$ . These  
403 values respected the biological constraint that extrinsic sources of excitation to brain regions  
404 are substantially weaker than intrinsic sources (Douglas & Martin (2007)). Further, these  
405 settings allowed  $k$  to encompass values between 1 and 3 found to be optimal in previous  
406 MEG and fMRI modelling studies (Hadida et al. (2018), Hellyer et al. (2016), Cabral et al.  
407 (2014), Deco & Jirsa (2012)). We set the prior distribution of  $IH_{scaling}$ , the inter-hemispheric  
408 scaling factor over the structural connectome, to  $2.5 \pm 0.5$ . These values reflected the known  
409 underestimation of long distance connections by diffusion MRI (Sotiropoulos & Zalesky  
410 (2019)). Further, these settings allowed  $IH_{scaling}$  to encompass values between 1.5 and 3.5  
411 found to be optimal in previous MEG modelling studies (Hadida et al. (2018)).

412

413 *Prior distributions of  $v$ ,  $delay$ ,  $coeffvar_{delay}$  and  $coef f_{balance}$*

414 Across the three methods, we estimated the matrix of inter-regional delays by element-wise  
415 division of the matrix of inter-regional distances by the matrix of conduction velocities.  
416 However, each method had a different set of parameters to estimate their corresponding  
417 matrix of conduction velocities, in accordance with that method's assumptions on spatial  
418 variation in conduction velocities (see Section 2.1). Hence, we set prior distributions for  
419 parameters specific to each of the three methods.

420

421 For the “distance-dependent delays” method, we had conduction velocity parameter  $v$ . We set  
422 the prior distribution of  $v$  to  $8 \pm 2$  m/s. We set the mean as 8 m/s to fall within the values  
423 between 5–11 m/s reported to be optimal across several MEG and fMRI modelling studies  
424 (Abey Suriya et al. (2018), Nakagawa et al. (2014), Cabral et al. (2014), Hellyer et al. (2016),  
425 Hadida et al. (2018)). We set the standard deviation to 2 m/s, so that values from the prior  
426 distribution of  $v$  would encompass central tendency values between 1.1 m/s and 7.4 m/s  
427 reported across human electrophysiological (Trebault et al. (2018), (Lemaréchal et al. (2022),  
428 Aboitiz et al. (1992)), macaque electrophysiological (Swadlow et al. (1978)) and macaque  
429 microscopy (Firmin et al. (2014)) studies. For the “isochronous delays” method, we had the  
430 mean delay parameter,  $delay$ , and a parameter controlling the coefficient of variation,  
431  $coeffvar_{delay}$ . We set the prior distribution of  $delay$  to  $10 \pm 3$  ms. We set the mean as 10 ms in  
432 line with the optimal “mean delay” across several MEG and fMRI modelling studies

433 (Abeyesuriya et al. (2018), Nakagawa et al. (2014), Cabral et al. (2014), Hellyer et al. (2016),  
434 Hadida et al. (2018)). We set the standard deviation to 3 ms, so that values from the prior  
435 distribution fell within the 1.5–24.9 ms range of inter-hemispheric delays reported across  
436 human and macaque electrophysiological studies (Aboitiz et al. (1992), Swadlow et al.  
437 (1978)). We set the prior distribution of  $coeffvar_{delay}$  to  $0.2 \pm 0.05$  respectively. We chose  
438 this setting so that low values from this parameter’s prior distribution would generate nearly  
439 identical conduction delays across connections, while high values would generate sets of  
440 inter-regional delays whose variation was similar to sets of distance-dependent delays. For  
441 the “mixed delays” method, we had the  $coef f_{balance}$  parameter. Values between 0 and 1  
442 indicated the relative proportion of isochronous delays and distance-dependent delays, 0  
443 indicating fully isochronous delays. We set the prior distribution of  $coef f_{balance}$  to  $0.5 \pm 0.15$ ,  
444 so that values from this parameter’s prior distribution generated sets of delays traversing the  
445 intermediate space between “distance-dependent” and “isochronous” sets of delays.  
446  
447 We refer the reader to our open dataset (Williams et al. (2023)) for time constants and spike  
448 thresholds of single studies, from which we estimated prior distributions of  $\tau_e$ ,  $\tau_i$ ,  $b_e$  and  $b_i$ .

## 449 2.3 Prior Predictive Checks

450 Prior Predictive Checks are performed to assess the suitability of the prior distributions and  
451 the model, before proceeding to fit the model to observed data (Gelman et al. (2013), van de  
452 Schoot et al. (2021), Gelman et al. (2020)). In the Prior Predictive Checks, we used different  
453 test statistics to determine if the range of dynamics generated by the BNM encompassed  
454 those we observed in the MEG resting-state data. We ran 1,000 simulations of each of the  
455 three BNMs with parameter values drawn from their respective joint prior distributions.  
456 Then, we estimated the values of four test statistics from the dynamics of each of the 1,000  
457 simulations and compared the sample medians of these test statistics, to the values of those  
458 test statistics on MEG resting-state data. We estimated the following test statistics: i) median  
459 of alpha-band phase synchronization strengths between all pairs of 148 brain regions, to  
460 measure central tendency in the strengths of phase synchronization, ii) median absolute  
461 deviation (MAD) of alpha-band phase synchronization strengths between all pairs of 148  
462 brain regions, to measure dispersion in the phase synchronization strengths, iii) mean of the  
463 Kuramoto order parameter (Kuramoto (1984), Breakspear et al. (2010)), to measure strength  
464 of zero-lag phase synchronization across the dataset, and iv) standard deviation of the



465 Kuramoto order parameter, to measure variability in zero-lag phase synchronization across  
466 the dataset. Please see Section 2.3.2 for details.

### 467 2.3.1 Processing experimental and simulated MEG data

468 We used eyes-open experimental MEG resting-state data from 75 subjects for ~600 seconds,  
469 at a sampling frequency of 1000 Hz. Data was collected with a 306-channel MEG system  
470 (204 planar gradiometers and 102 magnetometers, Elekta-MEGIN Oy) at HUS BioMag  
471 laboratory, Helsinki. Ethics approval was obtained from the Ethics Committee of Helsinki  
472 University Central Hospital. The study was performed according to the guidelines in the  
473 Declaration of Helsinki. Written informed consent was obtained from each participant prior  
474 to the study. Please see Siebenhühner et al. (2020) for further details.

475

476 We used temporal Signal Space Separation (Taulu & Hari (2009)) implemented in MaxFilter  
477 to suppress extra-cranial noise, and Independent Component Analysis (ICA) in FieldTrip  
478 (Oostenveld et al. (2011)), to remove artefacts of ocular, cardiac, or muscular origin.

479

480 We estimated subject-specific forward and inverse operators to map between source space  
481 and MEG sensor space, based on individual T1-weighted anatomical MRI scans that we  
482 collected at a resolution of  $1 \times 1 \times 1$  mm with a 1.5T MRI scanner (Siemens, Germany). We  
483 processed these MRIs with FreeSurfer (<http://surfer.nmr.mgh.harvard.edu/>) and used the  
484 dynamic Statistical Parametric Mapping (dSPM) method (Dale et al. (2000)) implemented in  
485 MNE (Gramfort et al. (2014)) to estimate inverse operators based on subject-specific head  
486 conductivity models and cortically constrained source models. We applied fidelity weighting  
487 to these inverse operators to reduce the influence of MEG field spread (Korhonen et al.  
488 (2014)). We applied these subject-specific inverse operators to MEG sensor-level data, to  
489 reconstruct dynamics at up to 7,500 sources per hemisphere for each subject. Next, we  
490 averaged the reconstructed dynamics within each brain region in the Destrieux atlas, to obtain  
491 the representative dynamics for each of the 148 regions. We then downsampled these source  
492 collapsed datasets of each subject to 250 Hz, before bandpass filtering in the alpha frequency  
493 band (8–12 Hz) with Morlet wavelets of peak frequency = 9.83 Hz and width parameter = 5.  
494 We chose a high value for the Morlet width parameter to account for subject-wise variability  
495 in the limits of the alpha frequency band (Haegens et al. (2014)). These operations yielded 75  
496 subject-specific alpha-band experimental MEG datasets, at the level of brain regions. From

497 30 of these subjects, we recorded another set of resting-state data. We used these 30  
498 additional MEG datasets to choose between the three BNMs with ABC model comparison.  
499 Further, we recorded eyes-closed MEG resting-state data from 28 of the original cohort of 75  
500 subjects. We used these 28 additional MEG datasets to choose between the three BNMs in  
501 eyes-closed MEG resting-state, where the compared BNMs had been fit to the original  
502 dataset of eyes-open MEG resting-state data from 75 subjects.

503

504 We generated simulated MEG data by first simulating the BNMs for 65 seconds at a  
505 sampling frequency of 250 Hz, before removing data from the first 5 seconds to remove the  
506 effect of transient dynamics. Then, we successively projected the simulated data to sensor-  
507 level with the same 75 subject-specific forward operators whose MEG data we recorded, and  
508 applied the 75 subject-specific inverse operators to the simulated sensor-level MEG data,  
509 resulting in 75 simulated source-space MEG datasets. Next, we performed the source  
510 collapsing and bandpass filtering of the simulated source-space MEG data identically as to  
511 the experimental MEG resting-state data, yielding 75 subject-specific alpha-band datasets of  
512 simulated MEG, across 148 brain regions of the Destrieux brain atlas.

### 513 2.3.2 Estimating test statistics for Prior Predictive Checks

514 For both simulated and experimental MEG datasets, we estimated the median and median  
515 absolute deviation (MAD) of phase synchronization strengths. To do this, we first estimated  
516 subject-specific matrices of phase synchronization between all pairs of 148 brain regions  
517 from the alpha-band source-space MEG datasets of each subject. We measured phase  
518 synchronization using weighted Phase Lag Index (wPLI), which is insensitive to the  
519 confounding influence of MEG field spread on estimates of phase synchronization (Vinck et  
520 al. (2011), Siebenhühner et al. (2016), Palva et al. (2018)). We estimated wPLI as:

521

$$522 \quad wPLI = \frac{|E(|\text{Imag}(X)|\text{sign}(\text{Imag}(X)))|}{E(|\text{Imag}(X)|)} \quad (3)$$

523

524 where  $X$  is the cross-spectrum between a pair of signals and  $\text{Imag}(X)$  is its imaginary  
525 component. We then averaged these subject-specific matrices along the subject dimension to  
526 obtain group-level matrices of phase synchronization. We estimated the median of phase  
527 synchronization strengths from the upper triangular elements of the group-level matrix of phase  
528 synchronization. We estimated the median absolute deviation (MAD) of phase synchronization

529 strengths as the median of absolute differences between each phase synchronization strength  
 530 and the median phase synchronization.

531

532 For both simulated and experimental source-space MEG datasets, we estimated the mean and  
 533 standard deviation of the Kuramoto order parameter  $R$ , by first estimating  $R$  at each time  $t$ :

534

$$535 \quad R(t) = \left| \frac{1}{N} \sum_{k=1}^N e^{i\phi_k(t)} \right| \quad (4)$$

536

537 where  $\phi_k(t)$  is the instantaneous phase of the oscillator with index  $k$ , and  $N$  is the total  
 538 number of oscillators. We estimated the mean and standard deviation of  $R(t)$  for the alpha-  
 539 band MEG dataset of each subject and then averaged these estimates across subjects, to  
 540 obtain group-level estimates of the strength and variability of zero-lag phase synchronization.  
 541 Please refer Table 1 for an overview of the test statistics we used, how we estimated them and  
 542 our purpose in using them.

543

Test statistic	Estimation	Purpose
Central tendency in strengths of inter-regional phase synchronization	Median of upper-triangular elements of group-level matrix of phase synchronization	To measure overall strength of inter-regional phase synchronization
Dispersion in strengths of inter-regional phase synchronization	Median Absolute Deviation (MAD) of upper-triangular elements of group-level matrix of phase synchronization	To measure overall variability of inter-regional phase synchronization
Strength of aggregate phase synchronization	Mean of subject-level means of Kuramoto order parameter	To measure strength of simultaneous, zero-lag phase synchronization across dataset
Temporal variability of aggregate phase synchronization	Mean of subject-level standard deviations of Kuramoto order parameter	To measure temporal variability of simultaneous, zero-lag phase synchronization across dataset

544 **Table 1.** Descriptions of each test statistic, their estimation and purpose.

## 545 2.4 BNM fitting

546 We used an ABC method, BOLFI (Bayesian Optimisation for Likelihood-Free Inference)  
547 (Gutmann & Corander (2016)) to fit each of the BNMs to experimental MEG data. We used  
548 the BOLFI implementation in the Python package, Engine for Likelihood Free Inference  
549 (ELFI) (Lintusaari et al. (2018)). We chose BOLFI to estimate BNM parameters since it is  
550 suitable for i) likelihood-free inference (LFI) settings where a model's intractable likelihood  
551 function renders standard likelihood-based methods inapplicable (Lintusaari et al. (2017)),  
552 and ii) high-dimensional inference, *i.e.* estimating more than ~10 model parameters - standard  
553 LFI methods such as ABC-Sequential Monte Carlo (SMC) (Sisson et al. (2007), West et al.  
554 (2021)) are only suitable to estimate a few model parameters and do not scale well to high-  
555 dimensional settings (Gutmann & Corander (2016)). BOLFI has been used to infer  
556 parameters of models in diverse fields, including genetics (Corander et al. (2017), McNally &  
557 Kallonen et al. (2019), Arnold et al. (2018)), cosmology (Leclercq (2018)), computational  
558 social science (Asikainen et al. (2020)) and cognitive science (Kangasrääsiö et al. (2019)).  
559 While a method similar to BOLFI has been used to estimate parameters of BNMs in Systems  
560 Neuroscience (Hadida et al. (2018)), it does not perform Bayesian inference - limiting its  
561 ability to include existing *e.g.*, neurophysiological constraints on values of BNM parameters,  
562 and to account for uncertainty in the values of BNM parameters when comparing BNMs.

563

564 BOLFI estimates posterior distributions of BNM parameters using Bayes' rule (Gelman et al.  
565 (2013)) to combine prior distributions of BNM parameters with an approximation of the  
566 BNM's likelihood function. We employed a Gaussian Process (GP)-based surrogate model to  
567 approximate the BNM's likelihood function. We trained the GP model with the results of  
568 multiple BNM simulations, to learn the mapping between combinations of parameter values  
569 and the corresponding discrepancies between BNM dynamics and MEG data. We used  
570 summary statistics to describe the BNM dynamics and MEG data. We used GPs due to their  
571 suitability in modelling smooth input-output relationships (Rasmussen & Williams (2006)) -  
572 we expected similar combinations of parameter values to generate similar BNM dynamics.  
573 Previously studied BNMs have demonstrated smooth input-output relationships (Hadida et al.  
574 (2018), Perl et al. (2020)). GPs acquire their smoothness constraint from their covariance  
575 matrix. We specify the functional form of the covariance matrix with a kernel, and we use a

576 kernel lengthscale parameter to quantify the rate of decrease in covariance with increases in  
577 values of BNM parameters. When used with BOLFI, GP surrogate models have drastically  
578 reduced the number of model simulations required to accurately estimate values of model  
579 parameters (Gutmann & Corander (2016)). Hence, we used BOLFI with GP surrogate models  
580 to fit high-dimensional BNMs of between 12 to 14 parameters in our study, to MEG data.

#### 581 2.4.1 BOLFI settings

582 We employed the following procedure and settings to apply BOLFI to estimate joint posterior  
583 distributions of each of the three BNMs. We set the prior distributions of parameters for each  
584 BNM as per the values we had specified (Section 2.2). We used the  $148 \times 148$  group-level  
585 matrix of static phase synchronization estimated from MEG resting-state (Section 2.3.2) to  
586 represent experimentally observed dynamics, against which we compared BNM dynamics.  
587 We chose to compare the group-level matrices of static phase synchronization estimated from  
588 the MEG data and BNM dynamics rather than corresponding descriptions of time-varying  
589 phase synchronization, due to i) the stable inter-regional patterns of phase synchronization  
590 across time reported in recent human electrophysiological studies (Nentwich et al. (2020),  
591 Mostame & Sadaghiani et al. (2021), Sadaghiani et al. (2022)), and ii) since comparing  
592 descriptions of time-varying phase synchronization returned by, *e.g.*, a HMM (Hidden  
593 Markov Model)-based method (Vidaurre et al. (2018)) would add a layer of complexity to the  
594 BNM fitting by increasing the dimensionality of the summary statistics (Lintusaari et al.  
595 (2017)) by a multiplicative factor equal to the number of hidden states and introducing  
596 problems of “state matching” between hidden states estimated from the MEG data and BNM  
597 dynamics. We simulated the BNM at 10,000 combinations of parameter values drawn from  
598 the BNM’s joint prior distribution. From the dynamics of each BNM simulation, we  
599 estimated  $148 \times 148$  group-level matrices of phase synchronization. We chose the summary  
600 statistics to be the vector of upper-triangular elements of the  $148 \times 148$  group-level matrices  
601 and used the Structural Similarity Index (SSI) (Wang et al. (2004)) to measure the similarity  
602 between summary statistics of the BNM dynamics and those from MEG data. We used SSI to  
603 measure similarity due to i) it simultaneously comparing mean, standard deviation and  
604 pattern of values in two input vectors in contrast to alternative measures such as, *e.g.*, Pearson  
605 Correlation which only compares the pattern of values in two input vectors, ii) its  
606 demonstrated effectiveness in comparing empirical brain functional networks to those  
607 generated by BNMs (Piccinini et al. (2021)) and generative models (Perl et al. (2020)), and

608 iii) its reported good performance in comparing high-dimensional images in image  
609 processing applications (Ledig et al. (2017), Dong et al. (2015), Wang et al. (2004a)), which  
610 is analogous to our comparing high-dimensional vectors of phase synchronization strengths.  
611 We estimated SSI as:

612

$$613 \quad SSI(x, y) = \frac{(2\mu_x\mu_y + C1)(2\sigma_x\sigma_y + C2_y)}{(\mu_x^2 + \mu_y^2 + C1)(\sigma_x^2 + \sigma_y^2 + C2)} \quad (5)$$

614

615 where  $\mu_x$ ,  $\mu_y$ ,  $\sigma_x$ ,  $\sigma_y$  and  $\sigma_x\sigma_y$  are local means, local standard deviations and cross-covariances  
616 of the vectors  $x$  and  $y$  respectively, and  $C1 = 0.01^2$  and  $C2 = 0.03^2$ .  $x$  and  $y$  were respectively  
617 the vectors of phase synchronization strengths estimated from BNM dynamics and MEG  
618 data. SSI values typically fall between 0 and 1, values close to 1 indicating highly similar  
619 vectors (Wang et al. (2004)). We expressed the discrepancy between summary statistics from  
620 MEG data and BNM dynamics as  $\ln(1 - SSI)$ . Hence, the discrepancy value for identical  
621 vectors would be  $-\infty$ . We applied the natural logarithm to provide finer resolution at low  
622 discrepancy values (Gutmann & Corander (2016)). A single BNM simulation can exceed 24  
623 hours, hence simulating BNMs at 10,000 combinations of parameter values in a serial manner  
624 would have prohibitively long run-time. We reduced computational run-time by exploiting  
625 the independence of BNM simulations, using an “embarrassingly parallel” paradigm on a  
626 HPC cluster to simulate BNMs at each of the 10,000 samples. We used “array jobs” to run  
627 the 10,000 simulations in 2,000 sets of 5 simulations, wherein we set the time limit for each  
628 set to 120 hours and the RAM memory limit to 30 GB. However, note that running BNM  
629 simulations in this manner only permitted training the GP model with combinations of  
630 parameter values drawn from their joint prior distributions. We did not run BNM simulations  
631 at points suggested by a Bayesian Optimisation (BO) acquisition function, *i.e.*, we did not  
632 have an active learning stage in the GP training. Since BNM simulations are not independent  
633 of each other during active learning, including an active learning stage would make  
634 computational run-times prohibitively long. We used an ARD (Automatic Relevance  
635 Determination) squared exponential kernel with a constant basis function to specify the  
636 functional form for the covariance matrix of the GP surrogate model. Algorithmic complexity  
637 of fitting the GP model scales as a cube of the number of simulations (Gutmann & Corander  
638 (2016)), hence fitting the GP model to  $\sim 10,000$  points can be computationally expensive. To  
639 aid convergence, we first used the subset of data method (2,000 points) to fit the GP model  
640 and used the residual noise variance estimated from this fit as a fixed parameter when fitting

641 the GP model to ~10,000 points. Once the GP fitting was complete, we assessed the quality  
642 of the fit by estimating the Pearson Correlation between actual discrepancies and GP-  
643 predicted discrepancies. We also determined the relative importance of each BNM parameter  
644 in explaining the actual discrepancies, by computing  $\exp^{-lengthscales}$  of the estimated ARD  
645 kernel lengthscales. Next, we estimated the posterior distributions of BNM parameters by  
646 combining the GP-based likelihood function with prior distributions of the BNM parameters.  
647 To estimate posterior distributions, we used the NUTS method (Hoffman & Gelman (2014))  
648 to sample 1,000 points each, from 4 chains, with half these points being used for warm-up.  
649 We set the posterior defining threshold as the minimum of the GP-based mean discrepancy  
650 function (Gutmann & Corander (2016)), and set 0.8 as the target probability, which is within  
651 the recommended range for this value (Betancourt et al. (2014)). Finally, we assessed  
652 convergence of the posterior sampling stage by checking if the effective number of samples  
653 was  $> 100$  and  $\hat{R} < 1.05$ , for each of the BNM parameters (Vehtari et al. (2021)). Effective  
654 number of samples indicates the number of samples from the posterior after accounting for  
655 autocorrelation between samples (Geyer et al. (2011)), while the  $\hat{R}$  diagnoses “chain mixing”  
656 by comparing between-chain and within-chain estimates of model parameters - values close  
657 to 1 suggest the absence of “chain mixing”.

#### 658 2.4.2 Assessing sensitivity of discrepancies to values of BNM parameters

659 The accuracy of posterior distributions estimated by ABC methods are highly dependent on  
660 the sensitivity of the discrepancies between ‘simulated’ and ‘observed’ dynamics, to the  
661 values of the BNM parameters (Lintusaari et al. (2017), Sunnåker et al. (2013)). For BOLFI,  
662 the accuracy of the posterior distributions are also dependent on the sensitivity of the GP-  
663 predicted discrepancies to the values of BNM parameters. We used fake-data simulations to  
664 assess the sensitivity of the actual and GP-predicted discrepancies, to values of two BNM  
665 parameters  $w_{ee}$  and  $w_{ei}$ . For these fake-data simulations, we used the same BNM as specified  
666 in Section 2.1, but with “instantaneous delays” or “zero delays” - using instantaneous delays  
667 allowed us to run the BNM simulations several orders of magnitude faster since we were  
668 solving ordinary differential equations rather than delay differential equations. We first  
669 generated a reference dataset of ‘observed’ dynamics by selecting a combination of parameter  
670 values producing oscillatory dynamics. We used the following values:  $w_{ee} = 12.9$ ,  $w_{ei} = 13.4$ ,  
671  $w_{ie} = 12.4$ ,  $w_{ii} = 0.85$ ,  $b_e = 2.85$ ,  $b_i = 4.7$ ,  $\tau_e = 15.9$ ,  $\tau_i = 18.1$ ,  $k = 1.6$ ,  $IH_{scating} = 2.83$  and  
672  $\psi_{sigma} = 0.13$ . We simulated the BNM with these parameter values 1,000 times with ODE45

673 (Bogacki & Shampine (1996)), other settings being identical to that specified in Section  
674 2.1.2. For each of the 1,000 simulations, we generated group-level matrices of phase  
675 synchronization, then averaged across these 1,000 group-level matrices to generate the  
676 reference group-level matrix of phase synchronization. Next, we generated datasets of  
677 ‘simulated’ dynamics by running 20 BNM simulations at every point in the  $100 \times 100$  grid  
678 defined by every pairwise combination of  $w_{ee}$  and  $w_{ei}$  values. We varied  $w_{ee}$  and  $w_{ei}$  across  
679 100 equally spaced points from 10 to 30 and from 6 to 30 respectively. We fixed values of all  
680 other BNM parameters to the same value as for the reference dataset. From the datasets of  
681 ‘simulated’ dynamics, we generated 20 group-level matrices of phase synchronization for  
682 every point in the  $100 \times 100$  grid, and averaged across these 20 repetitions to obtain a single  
683 group-level matrix at each point in the  $100 \times 100$  grid. Then, we estimated discrepancies  
684 between the reference ‘observed’ summary statistics and ‘simulated’ summary statistics at  
685 every point on the  $100 \times 100$  grid. We then determined if the discrepancy surface reached a  
686 global minimum at the point on the grid representing the combination of true values of  $w_{ee}$   
687 and  $w_{ei}$ . Further, we estimated a GP surrogate model relating the BNM parameter values to  
688 the corresponding discrepancies. We determined if the surface of GP-predicted discrepancies  
689 reached a global minimum at the point on the grid representing the combination of true  
690 values of  $w_{ee}$  and  $w_{ei}$ . These investigations revealed if the actual and GP-predicted  
691 discrepancies were sensitive to the values of two BNM parameters,  $w_{ee}$  and  $w_{ei}$ .

## 692 2.5 BNM evaluation

693 We evaluated the three fitted BNMs by comparing the posterior distributions of each of the  
694 BNM parameters to their respective prior distributions. Comparing the posterior distributions  
695 of BNM parameters to their prior distributions revealed additional constraints on the values  
696 of these parameters learnt from the MEG data, through BOLFI model fitting. Further, we ran  
697 Posterior Predictive Checks to assess the similarity between dynamics from the fitted BNMs  
698 and those reflected by the phase synchronization phenomena in the observed MEG data.

### 699 2.5.1 Posterior Predictive Checks

700 We used Posterior Predictive Checks (Gelman et al. (2013), Gelman et al. (2020), van de  
701 Schoot et al. (2021)) to determine if the dynamics generated by the three fitted BNMs  
702 correspond to those reflected by the phase synchronization phenomena in the MEG data. We  
703 ran 1,000 simulations of each of the three BNMs with parameter values drawn from their



704 respective joint posterior distributions. Just as for the Prior Predictive Checks (Section 2.3),  
705 we then estimated the values of four test statistics from the dynamics of each of the 1,000  
706 BNM simulations and compared the sample medians of these test statistics to the values of  
707 those test statistics on experimental MEG resting-state data. We used the same set of test  
708 statistics as for the Prior Predictive Checks: i) median of alpha-band phase synchronization  
709 strengths between all pairs of 148 brain regions, ii) median absolute deviation (MAD) of  
710 alpha-band phase synchronization strengths between all pairs of 148 brain regions, iii) mean  
711 of Kuramoto order parameter, and iv) standard deviation of Kuramoto order parameter (see  
712 Table 1 for details).

## 713 2.6 BNM comparison

714 We used standard ABC model comparison to compare the fitted BNMs with “isochronous  
715 delays”, “mixed delays”, and “distance-dependent delays”. We simulated the three BNMs,  
716 each with 1,000 sets of parameter values drawn from their respective joint posterior  
717 distributions. We simulated the BNMs at samples from their joint posterior distributions  
718 rather than their joint prior distributions since the posteriors represent probable values of  
719 BNM parameters after combining information from both previous neurophysiology  
720 experiments and our own MEG data. In contrast, the priors represent probable values of  
721 BNM parameters based only on information from previous neurophysiological experiments.  
722 Hence, the posteriors are more likely than the priors to reflect the ground-truth values of the  
723 BNM parameters. It follows from this that comparing the BNMs with samples from their  
724 respective posterior distributions enables isolating the influence of delays-related BNM  
725 parameters by reducing the potentially confounding effect of inaccurate estimates of other  
726 BNM parameters on the model comparison. For each of the three BNMs, we estimated  
727 discrepancies between dynamics from each of the 1,000 simulations to dynamics from an  
728 independent dataset of MEG resting-state data ( $N = 30$ ). We estimated discrepancy as  $\ln(1 -$   
729  $SSI)$ , identical to the original BNM fitting (Section 2.4.1). SSI is the Structural Similarity  
730 Index between the vectors of inter-regional phase synchronization strengths from BNM  
731 dynamics and MEG data. We estimated probability of each BNM by the relative acceptance  
732 rate of discrepancies associated with that BNM, with respect to a specified minimum  
733 discrepancy (Beaumont (2019)). We estimated model probabilities for a range of minimum  
734 discrepancies between -1 and 0, where -1 corresponded to a conservative threshold accepting  
735 very few discrepancy values across BNMs while 0 corresponded to a liberal threshold. We

736 then chose between the three BNMs based on the model probabilities across a range of  
737 discrepancy thresholds.

738

739 We refer the reader to our GitHub repository for the Python and MATLAB code, and  
740 SLURM scripts ([https://github.com/nitinwilliams/eeg\\_meg\\_analysis/tree/master/MEGMOD](https://github.com/nitinwilliams/eeg_meg_analysis/tree/master/MEGMOD)),  
741 that we used to simulate, fit and compare the BNMs. Within the GitHub repository, please  
742 check `file_descriptions.txt` for names of files implementing 1.) MATLAB functions to  
743 simulate each of the three BNMs – we called each of these functions via “array jobs”  
744 implemented in SLURM scripts (to be run on HPC resources), which we also make available,  
745 2.) MATLAB code to estimate the input set of parameter values and output set of  
746 discrepancies for BOLFI model fitting, for each BNM, 3.) Python code to use the ELFI  
747 toolkit to fit each of the BNMs to MEG resting-state data with BOLFI, 4.) MATLAB code to  
748 generate the set of posterior distributions returned by BOLFI in the correct order and scale,  
749 5.) MATLAB functions to simulate each of the three BNMs with samples from their posterior  
750 distributions – we called each of these functions via “array jobs” implemented in SLURM  
751 scripts (to be run on HPC resources), which we also make available, and 6.) MATLAB code  
752 implementing ABC model comparison to compare the three fitted BNMs.

### 753 3. Results

754 We compared the “isochronous delays”, “mixed delays”, and “distance-dependent delays”  
755 methods of specifying inter-regional delays in BNMs of alpha-band networks of phase  
756 synchronization. We specified BNMs implementing each of the three methods and then used  
757 an ABC workflow to adjudicate between them. The steps we followed were: i) we employed  
758 constraints from previous human and animal electrophysiological studies as well as the MEG  
759 and fMRI modelling literature, to specify prior distributions for parameters of each BNM, ii)  
760 we used Prior Predictive Checks to determine whether each of the BNMs, constrained by  
761 their prior distributions, generated dynamics encompassing those reflected by the phase  
762 synchronization phenomena in the MEG data, iii) we used fake-data simulations to verify that  
763 the estimated discrepancies between BNM dynamics and MEG data, were sensitive to the  
764 values of two BNM parameters, iv) we applied BOLFI to fit each of three BNMs to MEG  
765 resting-state data ( $N = 75$ ), yielding posterior distributions of their parameters, v) we  
766 employed Posterior Predictive Checks to verify that the fitted BNMs generated dynamics  
767 corresponding closely to those observed in the MEG dataset they were trained on, and vi) we

768 applied ABC model comparison to determine which of the three fitted BNMs generated  
 769 alpha-band networks of phase synchronization most similar to those observed in an  
 770 independent MEG resting-state dataset ( $N = 30$ ).

### 771 3.1 Prior specification

772 We combined the prior distribution of BNM parameters with an approximation of the BNM  
 773 likelihood function to estimate the posterior distributions of BNM parameters. Hence, using  
 774 biologically plausible, well-motivated prior distributions was important to accurately  
 775 estimating the posterior distributions of BNM parameters. We set prior distributions of BNM  
 776 parameters based on biological constraints, parameter values found to be optimal in the MEG  
 777 and fMRI modelling literature, and ranges of values generating oscillatory dynamics. We set  
 778 the priors to be Gaussian distributed and list their means and standard deviations below,  
 779 along with brief rationales for choosing these values (Table 2). We refer the reader to  
 780 Materials & Methods, Section 2.2 (see Figure 2) for a detailed description of the prior  
 781 specification.  
 782

Parameter (description)	Mean $\pm$ SD (units)	Rationale
$w_{ee}$ (Connection strength within excitatory neuronal populations)	$20 \pm 5$ (a.u.)	i) Dense recurrent structural connectivity between ‘layer 2/3 pyramidal neurons’ (Binzegger et al. (2004), Douglas et al. (1989), Douglas & Martin (2007), Jansen & Rit (1995)) ii) Similar strength of functional connections to those between excitatory and inhibitory neuronal populations <i>i.e.</i> , $w_{ei}$ and $w_{ie}$ (Seeman & Campagnola et al. (2018), Campagnola & Seeman et al. (2022)) iii) Encompasses range of values generating oscillatory dynamics
$w_{ei}$ (Connection strength from inhibitory to excitatory neuronal populations)	$18 \pm 6$ (a.u.)	i) Weaker strength of structural connections compared to dense connectivity within excitatory neurons (Binzegger et al. (2004), Douglas & Martin (2007)) ii) Similar strength of functional connections to those within excitatory neurons and from excitatory to inhibitory neurons <i>i.e.</i> , $w_{ee}$ and $w_{ie}$ (Seeman & Campagnola et al. (2018), Campagnola & Seeman et al. (2022)) iii) Encompasses range of values generating oscillatory dynamics

$w_{ie}$ (Connection strength from excitatory to inhibitory neuronal populations)	$18 \pm 6$ (a.u.)	i) Weaker strength of structural connections compared to dense connectivity within excitatory neurons (Binzegger et al. (2004), Douglas & Martin (2007)) ii) Similar strength of functional connections to those within excitatory neurons and from excitatory to inhibitory neurons <i>i.e.</i> , $w_{ee}$ and $w_{ie}$ (Seeman & Campagnola et al. (2018), Campagnola & Seeman et al. (2022)) iii) Encompasses range of values generating oscillatory dynamics
$w_{ii}$ (Connection strength within inhibitory neuronal populations)	$1 \pm 0.2$ (a.u.)	Sparse recurrent structural connectivity between inhibitory neurons (Markram et al. (2004), Binzegger et al. (2004))
$b_e$ (Firing threshold of excitatory neuronal populations)	$3 \pm 1$ (a.u.)	Low positive value since neurons fire in response to small, net excitation
$b_i$ (Firing threshold of inhibitory neuronal populations)	$5 \pm 1$ (a.u.)	i) Low positive value since neurons fire in response to small net excitation ii) Spike thresholds of inhibitory neurons are higher than spike thresholds of excitatory neurons, across all studies reported in NeuroElectro database
$\tau_e$ (Time constant of excitatory neuronal populations)	$18.6 \pm 3.6$ (ms)	Time constants of ‘layer 2/3 pyramidal neurons’ across studies in NeuroElectro database
$\tau_i$ (Time constant of inhibitory neuronal populations)	$15.1 \pm 4.7$ (ms)	Time constants of ‘basket cells’, ‘double bouquet cells’, ‘chandelier cells’, ‘Martinotti cells’, ‘bipolar cells’ and ‘interneurons from deep cortical layers’ reported across all studies in NeuroElectro database
$k$	$1.5 \pm 0.5$ (a.u.)	i) Low positive value since extrinsic input to excitatory population much lower than intrinsic input (Douglas & Martin (2007))

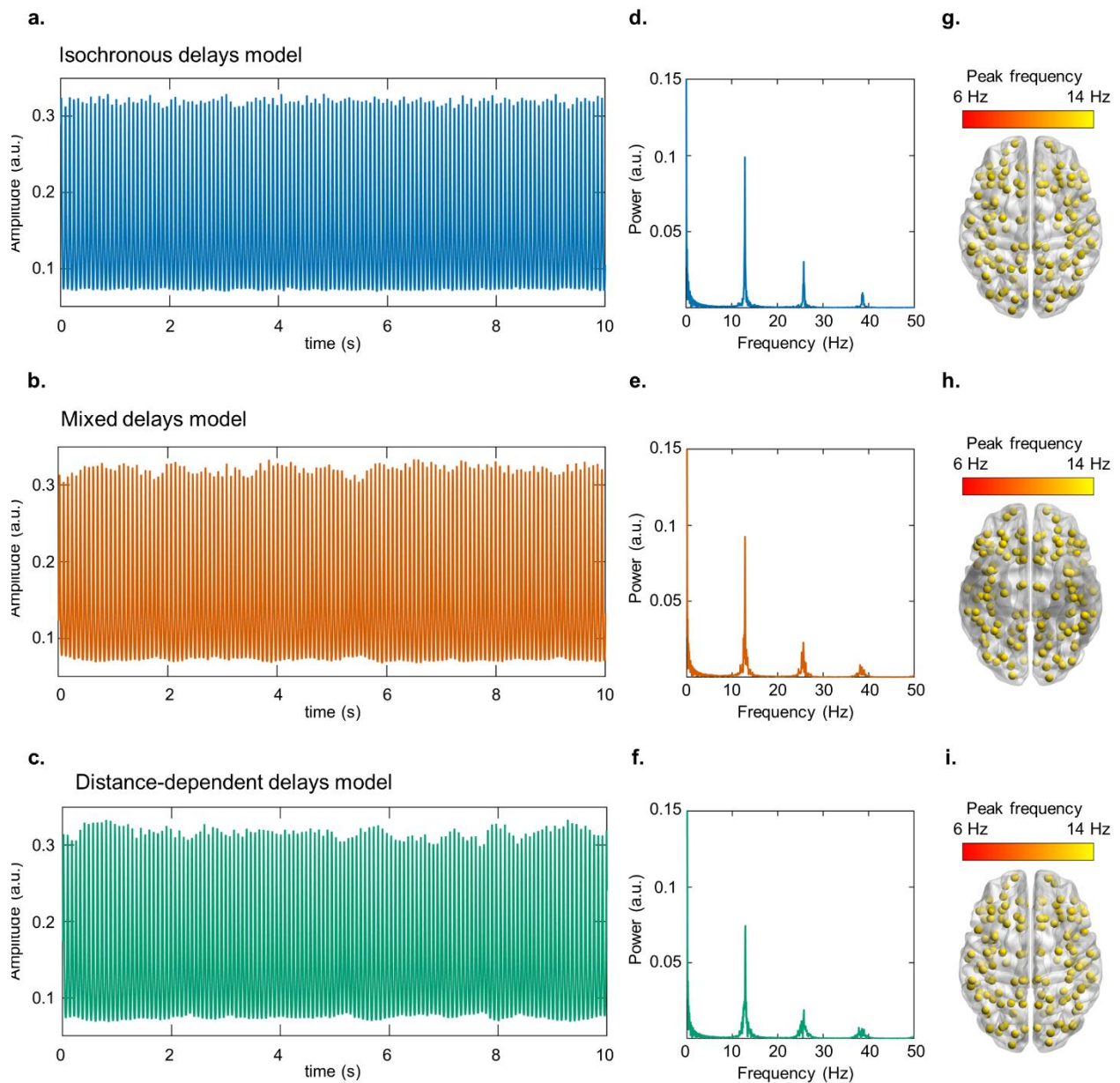
(Scalar multiplier over structural connectome)		ii) Encompassing range of values reported in MEG and fMRI modelling literature (Hadida et al. (2018), Hellyer et al. (2016), Cabral et al. (2014), Deco & Jirsa (2012))
$I_{H_{scaling}}$ (Inter-hemispheric scaling factor over structural connectome)	$2.5 \pm 0.5$ (a.u.)	i) Known under-estimation of long-distance connections by diffusion MRI (Sotiropoulos & Zalesky (2019)) ii) Encompassing range of values reported in MEG modelling literature (Hadida et al. (2018))
$\psi_{sigma}$ (Standard deviation of noise to excitatory and inhibitory populations)	$0.15 \pm 0.05$ (a.u.)	i) Positive value, much lower than firing thresholds of excitatory ( $b_e$ ) and inhibitory ( $b_i$ ) populations, since negligible probability of population firing due to noise input (Faisal et al. (2008)) ii) Encompassing range of values reported in MEG and fMRI modelling literature (Abey Suriya et al. (2018), Hellyer et al. (2016), Deco et al. (2009))
$v$ (Conduction velocity)	$8 \pm 2$ (m/s)	i) Within range of conduction velocities and corresponding axonal diameters reported in human and animal neuroanatomical and neurophysiological studies (Trebault et al. (2018), Lemaréchal et al. (2022), Swadlow et al. (1978)), Aboitiz et al. (1992), Firmin et al. (2014)) ii) Encompassing range of values reported in MEG and fMRI modelling literature (Abey Suriya et al. (2018), Nakagawa et al. (2014), Cabral et al. (2014), Hellyer et al. (2016), Hadida et al. (2018))
$delay$ (Mean conduction delay)	$10 \pm 3$ (ms)	i) Within range of inter-hemispheric delays reported in human and animal electrophysiological studies (Aboitiz et al. (1992), Swadlow et al. (1978)) ii) Encompassing range of values reported in MEG and fMRI modelling literature (Abey Suriya et al. (2018), Nakagawa et al. (2014), Cabral et al. (2014), Hellyer et al. (2016), Hadida et al. (2018))
$coeffvar_{delay}$ (Coefficient of variation in conduction delays)	$0.2 \pm 0.05$ (a.u.)	i) Low values of parameter would generate sets of nearly identical inter-regional delays ii) High values of parameter would generate sets of inter-regional delays with similar variation to sets of “distance-dependent delays”
$coeff_{balance}$	$0.5 \pm 0.15$ (a.u.)	Specified to enable the “mixed delays” method to traverse the intermediate space between the

(Coefficient of balance between “distance-dependent” and “isochronous” delays)		“distance-dependent delays” and “isochronous delays” methods
--	--	--

783 **Table 2.** Means and standard deviations of prior distributions for each of the BNM  
784 parameters, along with brief rationales for choosing the specified values.

### 785 3.2 BNMs simulated at prior means generate alpha-band dynamics

786 A pre-requisite for alpha-band phase synchronization is alpha-band oscillatory dynamics  
787 from individual brain regions. Hence, we investigated if the BNMs generated oscillatory  
788 dynamics at alpha-band frequencies. To do so, we ran 10 second simulations of BNMs with  
789 “isochronous delays”, “mixed delays”, and “distance-dependent delays” at their respective  
790 prior means. Then, we determined the peak frequencies of their dynamics - oscillations  
791 manifest as peaks in frequency spectra. We found that each of the three BNMs generated  
792 oscillatory dynamics (Figure 3a–c) with mean amplitude of 0.15 and mean standard deviation  
793 of 0.08 across brain regions. These oscillatory dynamics had spectral peaks in alpha-band  
794 (Figure 3d–f), with peak frequencies of  $12.9 \pm 0.07$  Hz (mean±standard deviation),  $12.9 \pm 0.1$   
795 Hz and  $12.8 \pm 0.14$  Hz for BNMs with “isochronous delays”, “mixed delays” and “distance-  
796 dependent delays” respectively, across regions (Figure 3g–i). The mean peak frequencies of  
797 all BNMs fell within the  $10.3 \text{ Hz} \pm 2.8 \text{ Hz}$  distribution of alpha-band peak frequencies  
798 reported in experimental MEG data (Haegens et al. (2014)). Hence, the three BNMs  
799 simulated at their respective prior means generated alpha-band oscillations, fulfilling a pre-  
800 requisite to investigate large-scale, alpha-band networks of phase synchronization.



801  
802 **Figure 3. BNMs simulated at prior means generate alpha-band oscillatory dynamics. a-**  
803 **c.** 10 s time course of dynamics from ‘left fronto-marginal gyrus and sulcus’ of BNMs with  
804 “isochronous delays”, “mixed delays”, and “distance-dependent delays” respectively. **d-f.**  
805 Frequency spectra of dynamics from ‘left fronto-marginal gyrus and sulcus’, of all three  
806 BNMs. **g-i.** Alpha-band peak frequencies of each region, of all three BNMs, in dorsal view.  
807 Plots on brain surface were visualised with BrainNet Viewer (Xia et al. (2013)).

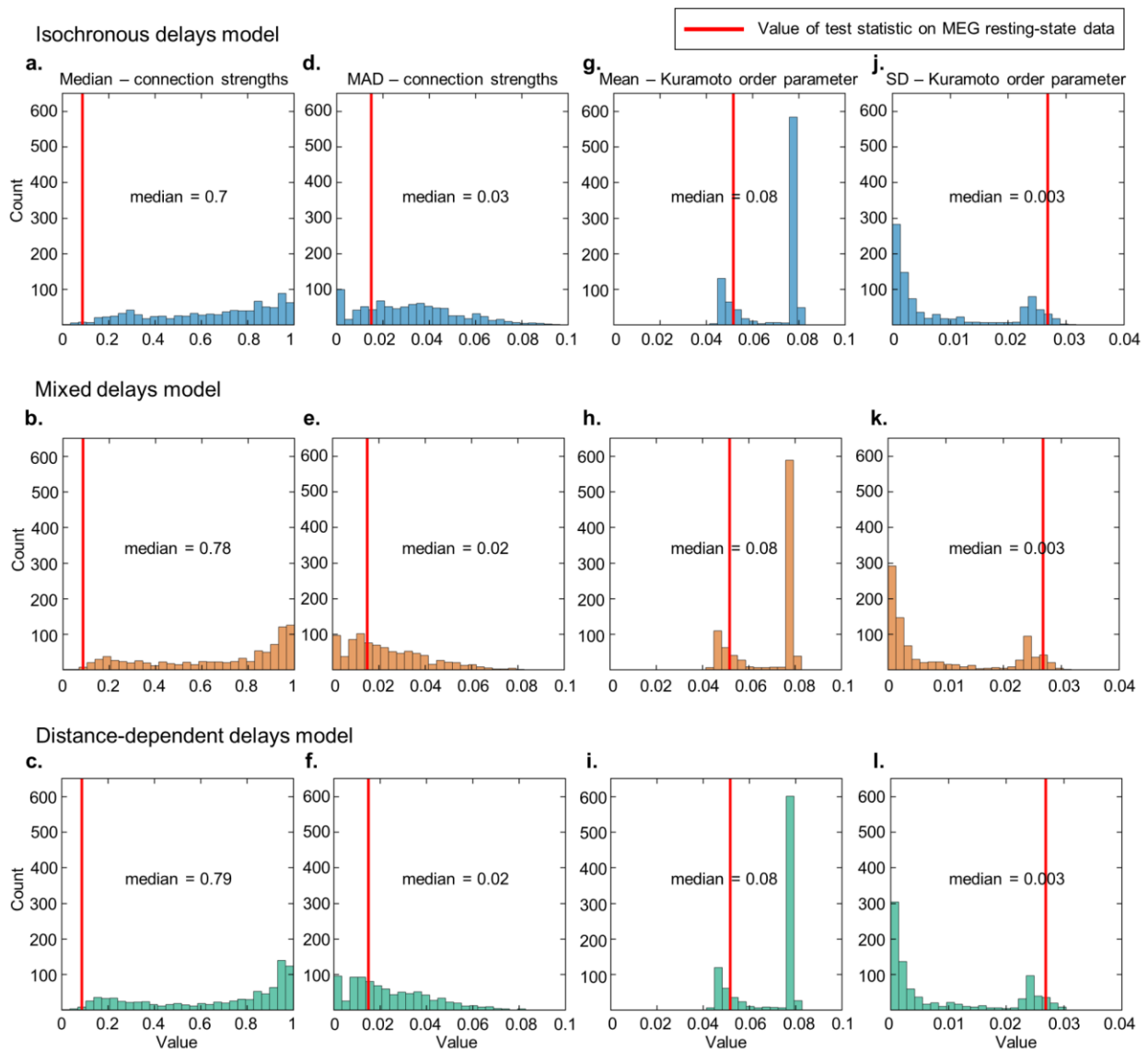
### 808 3.3 BNM dynamics encompass those observed in MEG data

809 The BOLFI fitting method assumes the suitability of the prior distributions of the BNM  
810 parameters and that the BNMs are not mis-specified. Hence, we performed Prior Predictive  
811 Checks to assess the ability of the BNMs, constrained by their prior distributions, to generate

812 the phase synchronization phenomena observed in MEG resting-state (Gelman et al. (2020),  
813 van de Schoot et al. (2021)). In addition, the Prior Predictive Checks allowed us to assess the  
814 similarity of the phase synchronization phenomena generated by the three BNMs, when these  
815 BNMs were constrained by their respective prior distributions. We performed the Prior  
816 Predictive Checks by comparing the sample medians of four test statistics that we estimated  
817 from 1,000 simulations of each of the BNMs, against the value of those same test statistics  
818 estimated on the experimental MEG dataset ( $N = 75$ ). We simulated the three BNMs with  
819 parameter values drawn from their joint prior distributions. As the test statistics, we used the  
820 median and median absolute deviation (MAD) of phase synchronization strengths between all  
821 region pairs, to measure their central tendency and dispersion respectively. We also estimated  
822 the mean and standard deviation of the Kuramoto order parameter, to measure overall  
823 strength and variability of zero-lag phase synchronization respectively (see Section 2.3.2 and  
824 Table 1 for details of each test statistic). We found that the values of each of the four test  
825 statistics estimated on the MEG dataset lay within the range of values of those test statistics  
826 estimated from the dynamics of each of the three BNMs (Figure 4a–l). The dispersion in  
827 strengths of inter-regional phase synchronization estimated on the MEG dataset was 0.02,  
828 which was close to the median values of 0.03, 0.02 and 0.02 for this test statistic, for the  
829 “isochronous delays”, “mixed delays”, and “distance-dependent delays” methods,  
830 respectively (Figure 4d–f). However, the central tendency of 0.09 for the strengths of inter-  
831 regional phase synchronization estimated on the MEG dataset was distant from the median  
832 values of 0.7, 0.78 and 0.79 for this test statistic, for the three methods, respectively (Figure  
833 4a–c). The mean and standard deviation of the Kuramoto order parameter had bimodal  
834 distributions for the sets of values estimated from dynamics of each of the three BNMs.  
835 Kuramoto mean and standard deviation close to 0.08 and 0 respectively, reflected parameter  
836 combinations for which the BNMs did not generate oscillatory dynamics while values close  
837 to 0.05 and 0.025 respectively, reflected parameter combinations for which the BNMs  
838 generated oscillatory dynamics. We found the values of 0.05 and 0.03 respectively, of these  
839 test statistics on the MEG dataset, to be close to their values for cases when the BNMs  
840 generated oscillatory dynamics (Figure 4g–l). The Prior Predictive Checks suggest that the  
841 three BNMs generate dynamics encompassing those reflected by the phase synchronization  
842 phenomena in MEG resting-state data. This suggests the suitability of the prior distributions  
843 of the BNM parameters and that the BNMs are not mis-specified, and hence can be fit to the  
844 MEG data with the BOLFI method. In addition, the correspondence between the three BNMs



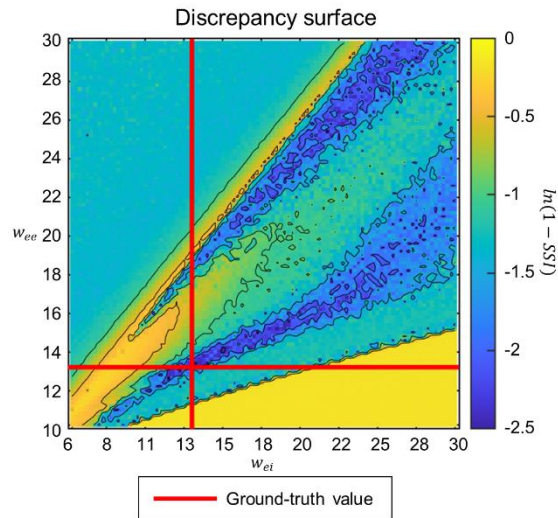
845 in the values of each of the test statistics (Figure 4a–l), suggested that each of the BNMs,  
 846 constrained by their prior distributions, generate similar phase synchronization phenomena.



847  
 848 **Figure 4. BNM dynamics encompass those observed in MEG data.** a-c. Histograms of  
 849 median of alpha-band phase synchronization strengths from multiple BNM simulations,  
 850 where parameter values were drawn from joint prior distributions of BNMs with  
 851 “isochronous delays”, “mixed delays”, and “distance-dependent delays” respectively. d-f.  
 852 Histograms of median absolute deviation (MAD) of alpha-band phase synchronization  
 853 strengths from multiple BNM simulations, of the three BNMs respectively. g-i. Histograms  
 854 of mean of Kuramoto order parameter from multiple BNM simulations, of the three BNMs  
 855 respectively. j-l. Histograms of standard deviation (SD) of Kuramoto order parameter from  
 856 multiple BNM simulations, of the three BNMs respectively. For all panels, the red line  
 857 indicates the corresponding value of that test statistic estimated from the MEG dataset.

### 858 3.4 Discrepancies between BNM dynamics and MEG data are 859 sensitive to values of BNM parameters

860 BOLFI returning accurate posterior distributions is highly dependent on whether the  
861 estimated discrepancies between BNM dynamics and MEG data are sensitive to values of the  
862 BNM parameters (Lintusaari et al. (2017), Sunnåker et al. (2013)). In the asymptotic case,  
863 BOLFI assumes the surface of discrepancies between summary statistics of BNM dynamics  
864 and MEG data to have a global minimum at the combination of true parameter values. We  
865 used fake-data simulations to assess this for two BNM parameters,  $w_{ee}$  and  $w_{ei}$ . To do so, we  
866 first generated the ‘observed’ summary statistics as the vector of phase synchronization  
867 strengths between all region pairs, averaged across 1,000 BNM simulations. We ran the BNM  
868 simulations with a pre-chosen set of parameters values, with  $w_{ee} = 12.9$  and  $w_{ei} = 13.4$ . Then,  
869 we generated ‘simulated’ summary statistics as the vector of phase synchronization strengths,  
870 averaged across 20 BNM simulations. We generated ‘simulated’ summary statistics at every  
871 point on a  $100 \times 100$  grid defined by every pair of  $w_{ee}$  and  $w_{ei}$  values, where we varied  $w_{ee}$   
872 from 10–30 and  $w_{ei}$  from 6–30. We fixed values of other BNM parameters to the same values  
873 used to generate the ‘observed’ summary statistics. Finally, we estimated the discrepancies as  
874  $\ln(1 - SSI)$  between the reference ‘observed’ summary statistics and the ‘simulated’ summary  
875 statistics at each point on the  $100 \times 100$  grid. SSI is the Structural Similarity Index. We also  
876 estimated a set of Gaussian Process (GP)-predicted discrepancies from a GP model trained  
877 with the set of actual discrepancies and corresponding BNM parameter values. We found that  
878 the surface of actual discrepancies reached a global minimum at the combination of the true  
879 parameter values, *i.e.*,  $w_{ee}=12.9$ ,  $w_{ei}=13.4$  (Figure 5). In addition, we found low discrepancies  
880 at points on the grid corresponding to high values of  $w_{ee}$  and  $w_{ei}$ , but these values were higher  
881 than the discrepancy value at the combination of true parameter values. For example, we  
882 estimated a discrepancy of -2.48 at the combination of true values ( $w_{ee}=12.9$ ,  $w_{ei}=13.4$ ),  
883 while we estimated a discrepancy of -2.06 at  $w_{ee}=27.6$ ,  $w_{ei}=24.2$ . Notably, the surface of GP-  
884 predicted discrepancies also reached a global minimum at the combination of the true  
885 parameter values (Figure S4). These results demonstrate the sensitivity of the discrepancies to  
886 the values of  $w_{ee}$  and  $w_{ei}$ , suggesting that BOLFI can return accurate posterior distributions of  
887 at least these two BNM parameters.



888

889 **Figure 5. Discrepancies are sensitive to values of BNM parameters** 100 × 100 grid of  
890 discrepancies between summary statistics of BNM dynamics at every pair of  $w_{ee}$  and  $w_{ei}$   
891 values, and BNM dynamics at  $w_{ee}=12.9$ ,  $w_{ei}=13.4$ .  $w_{ee}$  is the strength of connections within  
892 excitatory neuronal populations,  $w_{ei}$  is the strength of connections from inhibitory to  
893 excitatory neuronal populations. Red lines indicate ground-truth values of  $w_{ee}$  and  $w_{ei}$ .  
894 Discrepancies were measured by  $\ln(1 - SSI)$ . SSI is the Structural Similarity Index.

### 895 3.5 BOLFI yields BNM parameter estimates informed by MEG data

896 The behaviour of BNMs is highly dependent on the parameter values with which they are  
897 simulated. So, we first constrained values of the parameters of each of the three BNMs with  
898 MEG data, before proceeding to compare the three BNMs. To do so, we applied the high-  
899 dimensional inference method BOLFI (Gutmann & Corander (2016)), to fit each of the  
900 BNMs to MEG resting-state data ( $N = 75$ ). BOLFI uses standard Bayesian inference to  
901 combine the prior distributions of BNM parameters with an approximation of the BNM's  
902 likelihood function, to estimate posterior distributions of BNM parameters. BNMs typically  
903 have intractable likelihood functions, so BOLFI approximates these with Gaussian Process  
904 (GP) models trained on parameters values of multiple BNM simulations and the  
905 corresponding discrepancies between BNM dynamics and MEG data. We ran 10,000  
906 simulations of each of the three BNMs and trained GPs parameterised with ARD squared  
907 exponential kernels, on values of the BNM parameters and the corresponding discrepancies.  
908 We estimated discrepancies as  $\ln(1 - SSI)$  between the vectors of inter-regional phase  
909 synchronization strengths estimated from BNM dynamics and MEG data. SSI is the  
910 Structural Similarity Index (Wang et al. (2004)).

911 The multiple BNM simulations yielded 9004, 9063, and 9093 completed simulations of  
912 BNMs with “isochronous delays”, “mixed delays”, and “distance-dependent delays”  
913 respectively, the others exceeding the time limit or crossing the memory limit. These “out of  
914 memory” errors likely reflect the excessive memory demand due to very small step sizes  
915 taken by the solver when dealing with discontinuities in the solution of the system of  
916 differential equations representing each BNM. For the completed simulations, we found  
917 Pearson Correlations between actual and GP-predicted discrepancies of 0.58, 0.67 and 0.67,  
918 for BNMs with “isochronous delays”, “mixed delays”, and “distance-dependent delays”  
919 respectively (Figure S5a–c). These close correspondences suggested the GP-based models of  
920 each BNM to suitably approximate their likelihood functions. For all three BNMs, we found  
921 that parameters governing dynamics of individual brain regions had a strong influence on  
922 predicting the discrepancies between BNM dynamics and MEG data (Figure S5d–f). In  
923 particular, the strength of connections within excitatory neuronal populations ( $w_{ee}$ ), between  
924 excitatory and inhibitory populations ( $w_{ei}$  and  $w_{ie}$ ), and the firing thresholds of excitatory ( $b_e$ )  
925 and inhibitory populations ( $b_i$ ), had a strong influence. The influence of these parameters is  
926 consistent with neurophysiological studies on, *e.g.*, the role of reciprocal interaction between  
927 excitatory and inhibitory populations, in generating the oscillatory dynamics necessary for  
928 inter-regional phase synchronization (Buzsáki (2006), Traub (1997)). We also found that the  
929 parameter controlling the strength of inter-regional anatomical connections ( $k$ ) had an  
930 influence on predicting the discrepancies between BNM dynamics and MEG data. This is  
931 also consistent with understanding on the role of these connections in promoting inter-  
932 regional phase synchronization (Gray (1994)).

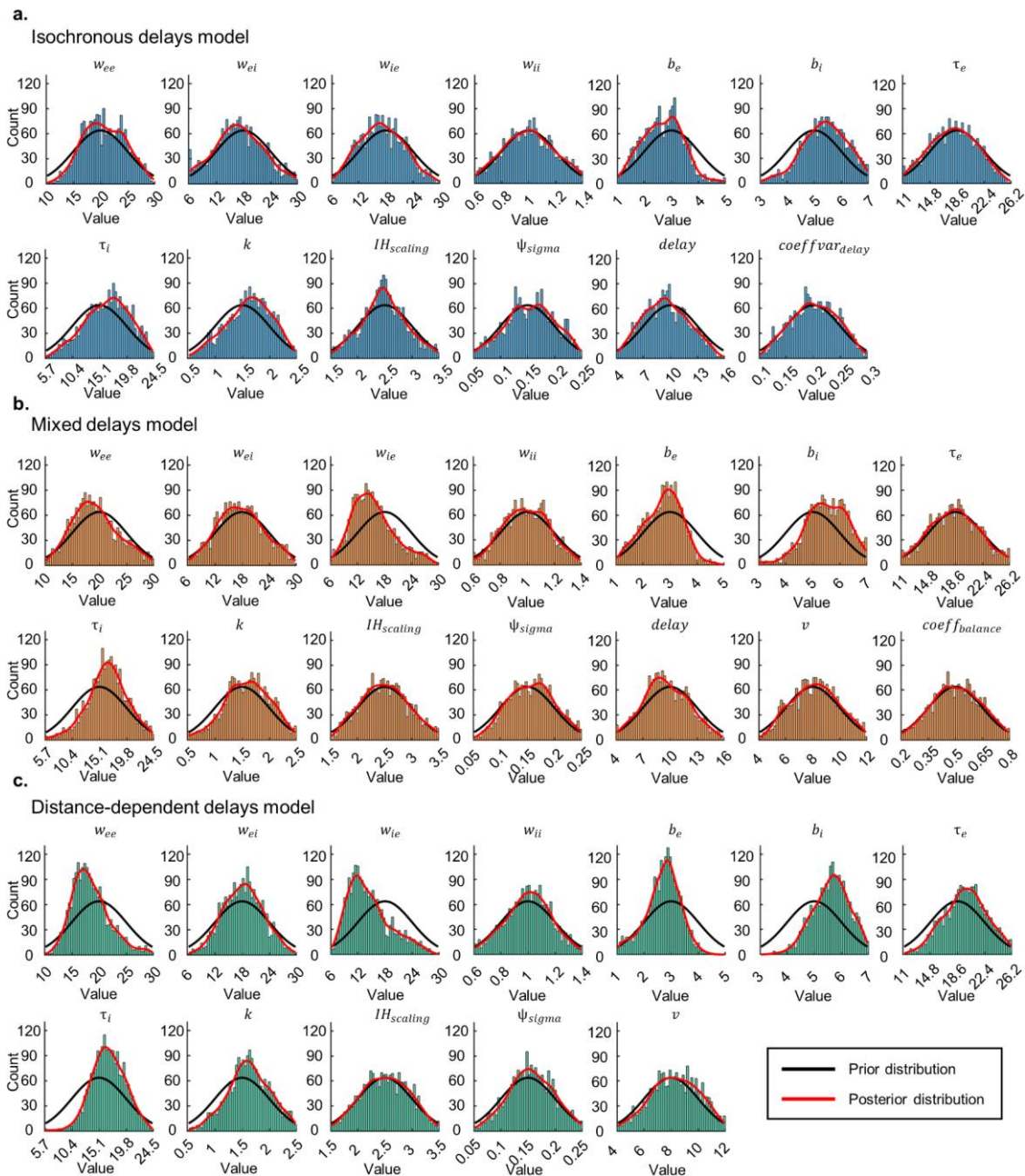
933

934 BOLFI yielded reliable posterior distributions of parameters of all three BNMs.  $\hat{R}$  values  
935 were lower than 1.05 for all parameters and effective numbers of samples exceeded 100  
936 (Vehtari et al. (2021)) for all but one parameter, *i.e.*,  $b_i$  in the BNM with “isochronous  
937 delays” which had 91 effective samples. For all three BNMs, the mass of the posterior  
938 distributions of  $b_e$  shifted toward lower values compared to their prior distributions while the  
939 mass of the posterior distributions of  $b_i$  shifted toward higher values (Figure 6a–c). For the  
940 BNM with “isochronous delays” for example, prior means for  $b_e$  and  $b_i$  were 3 and 5  
941 respectively, while their posterior means were 2.7 and 5.4 (Figure 6a). These posterior  
942 distributions of  $b_e$  and  $b_i$  across BNMs, are in agreement with neurophysiological constraints  
943 that spike thresholds of inhibitory neurons are higher than spike thresholds of excitatory  
944 neurons (see Figure 2b and Section 2.2 on Prior Specification). For all three BNMs, we also

945 observed the mass of the posterior distributions of  $\tau_i$ , time constant of inhibitory neuronal  
946 populations, to shift toward higher values compared to their prior distributions (Figure 6a–c).  
947 For the BNM with “isochronous delays” for example, prior mean for  $\tau_i$  was 15.1 ms while its  
948 posterior mean was 16.4 ms (Figure 6a). For BNMs with “mixed delays” and “distance-  
949 dependent delays”, mass of the posterior distributions of  $w_{ee}$  and  $w_{ie}$  shifted toward lower  
950 values (Figure 6b–c). For the BNM with the “distance-dependent delays” for example, prior  
951 means for  $w_{ee}$  and  $w_{ie}$  were 20 and 18 respectively, while their posterior means were 18.5 and  
952 14.5 (Figure 6c). Notably, the lower values of  $w_{ee}$  were in better agreement with empirical  
953 estimates of functional connectivity within excitatory neuronal populations (Seeman et al.  
954 (2018), Campagnola et al. (2022)) than corresponding estimates of structural connectivity  
955 (Jansen & Rit (1995), Douglas & Martin (2007), Douglas et al. (1989), Binzegger et al.  
956 (2004)). We also inspected posterior distributions of BNM parameters relating to inter-  
957 regional delays. For BNMs with “isochronous delays” and “mixed delays”, the posterior  
958 means of the delay parameter *delay* were shifted to 9.5 ms and 9.6 ms respectively, from their  
959 prior means of 10 ms (Figure 6a–b). Taken together, we found that applying BOLFI yielded  
960 reliably estimated posterior distributions of parameters of the three BNMs, which were in  
961 agreement with neurophysiological results. Hence, we could use these BNMs, constrained by  
962 MEG data, to choose between the three methods to specify inter-regional delays.

963

964 We note that the estimated posterior distributions could be used to specify BNMs in future  
965 modelling efforts. We refer the reader to our open dataset (Williams et al. (2023)), where we  
966 have made available the joint posterior distribution of each of the three BNMs, from which  
967 the marginal distributions that we report here, as well as their conditional distributions and  
968 joint distributions can be used to specify values of BNM parameters.



969

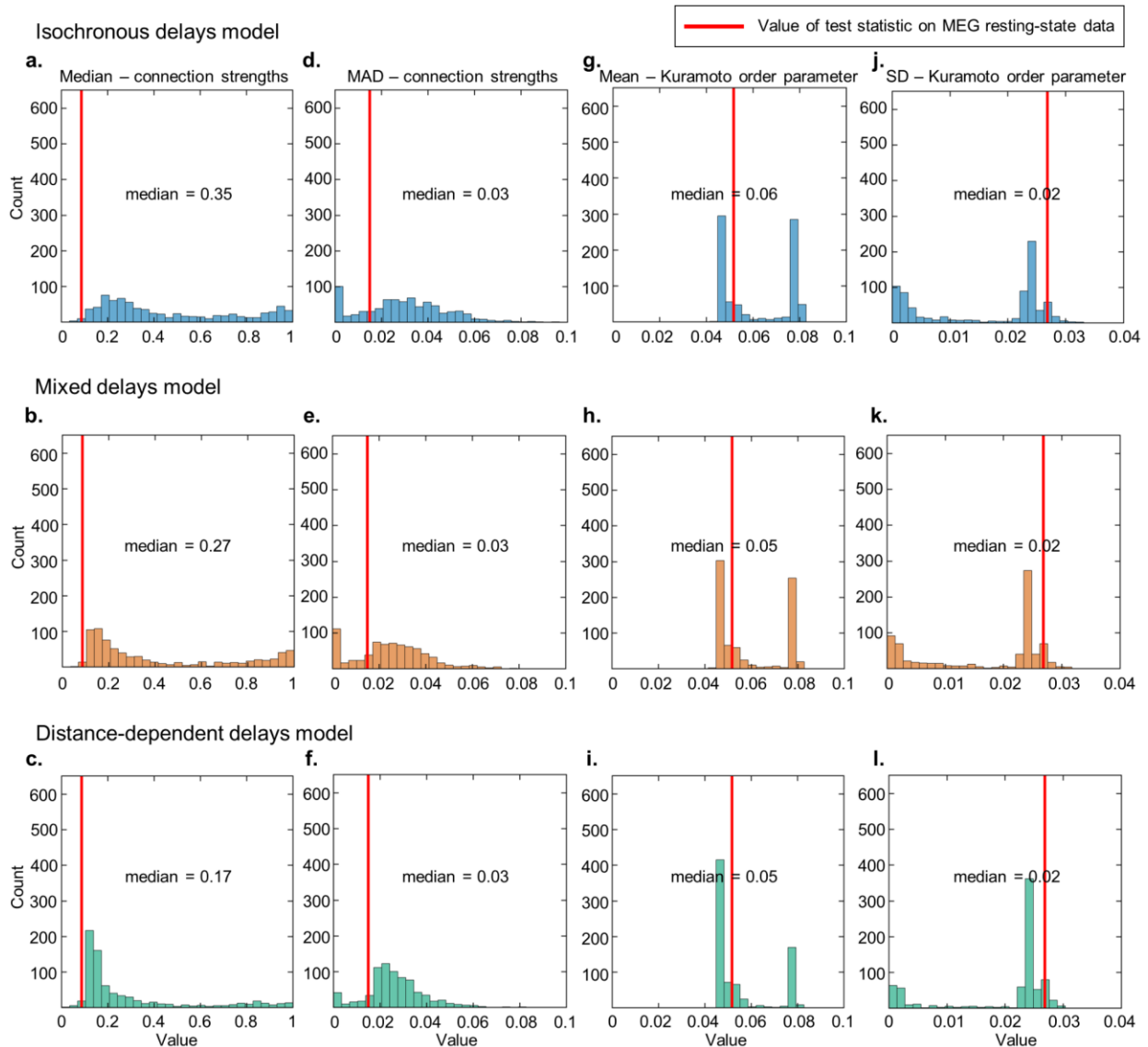
970 **Figure 6. BOLFI yields BNM parameter estimates informed by MEG data** a. Marginal  
 971 posterior distributions of BNM with “isochronous delays” b. Marginal posterior distributions  
 972 of BNM with “mixed delays” c. Marginal posterior distributions of BNM with “distance-  
 973 dependent delays”. Black lines indicate prior distributions, while red lines indicate kernel  
 974 density estimates of posterior distributions.

### 975 3.6 Fitted BNM dynamics correspond to those observed in MEG data

976 The procedure we used to compare the three BNMs assumed the absence of computational  
 977 problems when the BNMs were fit to MEG data. Hence, we used Posterior Predictive Checks  
 978 (Gelman et al. (2020), van de Schoot et al. (2021)) to evaluate the fitted BNMs, before

979 comparing them in the next stage. In addition, we used the Posterior Predictive Checks to  
980 assess the similarity of the phase synchronization phenomena generated by the three BNMs,  
981 when these BNMs were constrained by their respective posterior distributions. We performed  
982 the Posterior Predictive Checks by comparing sample medians of four test statistics that we  
983 estimated from 1,000 simulations of each of the fitted BNMs, against the value of those test  
984 statistics estimated on the MEG dataset. Identical to the Prior Predictive Checks (Section  
985 3.3), the test statistics that we used were the median and median absolute deviation (MAD) of  
986 phase synchronization strengths between all region pairs, to measure their central tendency  
987 and dispersion respectively. We also estimated the mean and standard deviation of the  
988 Kuramoto order parameter, to measure overall strength and variability of zero-lag phase  
989 synchronization respectively (see Section 2.3.2 and Table 1 for details of each test statistic).  
990 We found the sample medians of the four test statistics estimated on the dynamics of all three  
991 BNMs to correspond closely to the values of those test statistics on the MEG dataset (Figure  
992 7a–l). Just as for the Prior Predictive Checks, the value of 0.02 for dispersion in phase  
993 synchronization strengths in the MEG dataset was close to the median values of 0.03 for this  
994 test statistic across the three methods (Figure 7d–f). In contrast to the Prior Predictive Checks  
995 however, the value of 0.09 for central tendency in phase synchronization strengths in the  
996 MEG dataset was close to the values of 0.35, 0.27 and 0.17 for this test statistic, for the  
997 “isochronous delays”, “mixed delays”, and “distance-dependent delays” methods respectively  
998 (Figure 7a–c). The corresponding values from the Prior Predictive Checks were 0.7, 0.78 and  
999 0.79. These results suggest that compared to the mean strengths of phase synchronization  
1000 generated by the BNMs before fitting, those generated by the fitted BNMs were more similar  
1001 to those we observed in the MEG dataset while also being more different across BNMs. Just  
1002 as for the Prior Predictive Checks, the mean and standard deviation of the Kuramoto order  
1003 parameter had a bimodal distribution for the set of values estimated from the dynamics of all  
1004 three BNMs. In contrast to the Prior Predictive Checks however, the sample medians of these  
1005 test statistics were close to their values in the MEG dataset. The value for mean of the  
1006 Kuramoto order parameter was 0.06, 0.05 and 0.05 for the “isochronous delays”, “mixed  
1007 delays”, and “distance-dependent delays” methods respectively, which was close to 0.05 for  
1008 this test statistic in the MEG dataset (Figure 7g–i). Similarly, the value for standard deviation  
1009 of the Kuramoto order parameter was 0.02 across the three methods, close to the value of  
1010 0.03 for this test statistic in the MEG dataset (Figure 7j–l). Compared to the values of the test  
1011 statistics estimated on the dynamics of the BNMs before fitting, their values estimated on the  
1012 dynamics of the fitted BNMs corresponded more closely to the values of those test statistics

1013 in the MEG dataset. This suggests that compared to the prior distributions of the BNM  
 1014 parameters, their posterior distributions more accurately reflected the ground-truth values of  
 1015 the BNM parameters. Hence, the Posterior Predictive Checks suggested that all three BNMs  
 1016 were fit to the MEG data without computational problems, and that they could be used to  
 1017 choose between the three methods with ABC model comparison.



1018  
 1019 **Figure 7. Fitted BNM dynamics correspond to those observed in MEG data. a-c.**

1020 Histograms of median of alpha-band phase synchronization strengths from multiple BNM  
 1021 simulations, where parameter values were drawn from joint posterior distributions of BNMs  
 1022 with “isochronous delays”, “mixed delays”, and “distance-dependent delays” respectively. **d-**  
 1023 **f.** Histograms of median absolute deviation (MAD) of alpha-band phase synchroniza-  
 1024 tion strengths from multiple BNM simulations, of the three BNMs respectively. **g-i.** Histograms  
 1025 of mean of Kuramoto order parameter from multiple BNM simulations, of the three BNMs  
 1026 respectively. **j-l.** Histograms of standard deviation (SD) of Kuramoto order parameter from

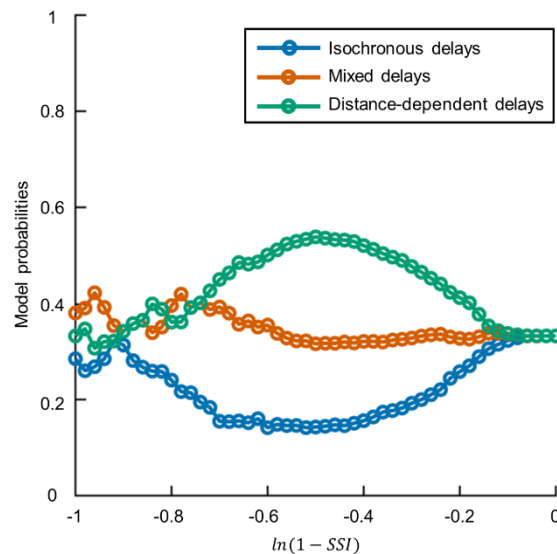


1027 multiple BNM simulations, of the three BNMs respectively. For all panels, the red line  
1028 indicates the corresponding value of that test statistic estimated from the MEG dataset.

### 1029 3.7 BNM with “distance-dependent delays” more probable than 1030 BNMs with “isochronous delays” and “mixed delays”

1031 Finally, we compared the three methods to specify inter-regional delays in BNMs of large-  
1032 scale networks of phase synchronization observed in MEG resting-state. Having fitted BNMs  
1033 implementing each of the methods to an MEG dataset ( $N = 75$ ), we used ABC model  
1034 comparison (Beaumont (2019), Sunnåker et al. (2013)) to choose between the fitted BNMs  
1035 with a separate MEG dataset ( $N = 30$ ). To do so, we first ran 1,000 simulations of each of the  
1036 three BNMs, with parameter values drawn from their respective joint posterior distributions.  
1037 For each of the three BNMs, we estimated discrepancies between BNM dynamics from each  
1038 of the simulations, and MEG data. We computed discrepancy as  $\ln(1 - SSI)$  between vectors  
1039 of phase synchronization strengths from BNM dynamics and MEG data. We then estimated  
1040 model probability of each BNM by the relative acceptance rate of discrepancies associated  
1041 with that BNM, with respect to a range of minimum discrepancies from -1 to 0. Model  
1042 probabilities represented how likely each of the BNMs were, to describe the generation of  
1043 large-scale, alpha-band, networks of phase synchronization seen in MEG resting-state data.  
1044 The multiple simulations yielded 807, 767 and 779 completed simulations for BNMs with  
1045 “isochronous delays”, “mixed delays”, and “distance-dependent delays” respectively, the  
1046 others exceeding the time limit or crossing the memory limit. The model comparison method  
1047 assumes equal numbers of simulations across BNMs, so we used only the first 767 completed  
1048 simulations of the three BNMs, *i.e.*, lowest number of completed simulations across BNMs.  
1049 Model probabilities of the BNM with “distance-dependent delays” were higher than those of  
1050 the BNMs with “isochronous delays” and “mixed delays”, across thresholds from -0.7 to -0.2  
1051 (Figure 8). For a threshold of -0.5 for example, the BNM with “distance-dependent delays”  
1052 had a probability of 0.54, while the BNM with “mixed delays” had a probability of 0.32 and  
1053 the BNM with “isochronous delays” had the lowest probability of 0.14. We found the higher  
1054 probabilities of the BNM with “distance-dependent delays” to be driven by the similarity  
1055 between its mean strengths of phase synchronization to that observed in the MEG data, rather  
1056 than the similarity in its standard deviation or its pattern of phase synchronization strengths to  
1057 those observed empirically (Figure S6). We found the three BNMs to be similarly probable at  
1058 low thresholds close to 0 and high thresholds close to 1. However, the very low and very high

1059 numbers of accepted simulations at these thresholds respectively, render their probabilities  
1060 non-informative. Notably, we observed an identical pattern of results at intermediate  
1061 discrepancy thresholds when using eyes-closed MEG resting-state data in the ABC model  
1062 comparison, inspite of the BNMs being fit to eyes-open MEG resting-state data (Figure S7).  
1063 Hence, the ABC model comparison revealed the BNM with “distance-dependent delays” as  
1064 the most probable and the BNM with “isochronous delays” as the least probable, of  
1065 describing the generating of large-scale networks of phase synchronization seen in MEG.



1066  
1067 **Figure 8. BNM with “distance-dependent delays” more probable than BNMs with**  
1068 **“isochronous delays” and “mixed delays”.** Model probabilities of BNMs with “isochronous  
1069 delays”, “mixed delays”, and “distance-dependent delays”, for a range of minimum  
1070 discrepancies between phase synchronization strengths of BNM dynamics and MEG data.  
1071 Discrepancies are estimated as  $\ln(1 - SSI)$ , where SSI is the Structural Similarity Index.

1072  
1073 While the three BNMs differed in the extent to which distance between brain regions  
1074 determined the inter-regional delays, they also differed in the variability or heterogeneity of  
1075 their delays. BNMs with “distance-dependent delays” had the highest delay heterogeneity.  
1076 Hence, we performed a control analysis to assess whether the correspondence between phase  
1077 synchronization strengths of the BNM with “distance-dependent delays” and those in MEG  
1078 data arose merely from delay heterogeneity. To do so, we ran 1,000 simulations of a BNM  
1079 with “randomised delays”, where we used randomly resampled (without replacement)  
1080 versions of “distance-dependent delays” used in the ABC model comparison. We simulated  
1081 the BNM with “randomised delays” at the same parameter values we had used to simulate the  
1082 BNM with “distance-dependent delays” in the ABC model comparison. Then, we estimated

1083 discrepancies between dynamics of the BNMs with “randomised delays” and MEG data, and  
1084 used a Wilcoxon rank-sum test to compare these to the corresponding discrepancies for the  
1085 BNMs with “distance-dependent delays”. We found the discrepancies for the BNM with  
1086 “distance-dependent delays” to be much lower ( $p = 4.5e^{-46}$ ) than those for the BNM with  
1087 “randomised delays” (Figure S8). The sample median of discrepancies for the BNM with  
1088 “distance-dependent delays” was -0.41, while the sample median of discrepancies for the  
1089 BNM with “randomised delays” was -0.22. Hence, the control analysis revealed that mere  
1090 delay heterogeneity does not account for the correspondence between inter-regional phase  
1091 synchronization strengths of the BNM with “distance-dependent delays” and those in MEG  
1092 data. These results rule out alternative explanations for the BNM with “distance-dependent  
1093 delays” being more probable than BNMs with “isochronous delays” and “mixed delays”, of  
1094 describing the generation of large-scale networks of phase synchronization seen in MEG.

## 1095 4. Discussion

1096 Large-scale networks of phase synchronization are considered to regulate communication  
1097 between brain regions, but the relationship to their structural substrates remains poorly  
1098 understood. In this study, we used an ABC workflow to compare the “isochronous delays”,  
1099 “mixed delays”, and “distance-dependent delays” methods of specifying inter-regional delays  
1100 in BNMs of phase synchronization. Prior Predictive Checks revealed BNMs of all three  
1101 methods to generate phase synchronization phenomena encompassing those observed in  
1102 MEG resting-state. Fitting the BNMs to MEG resting-state data yielded reliable posterior  
1103 distributions of parameters of all the three BNMs. Finally, ABC model comparison of the  
1104 fitted BNMs revealed the BNM with “distance-dependent delays” to be the most probable to  
1105 describe the generation of large-scale networks of phase synchronization seen in MEG.

1106

1107 Previous modelling studies have demonstrated the role of distance-dependent inter-regional  
1108 delays in generating power spectra of MEG activity from individual brain regions (Cabral et  
1109 al. (2022)), alpha-band inter-regional networks of amplitude correlation (Cabral et al. (2014),  
1110 Nakagawa et al. (2014)), and the observed bimodal distribution (Dotson et al. (2014), Dotson  
1111 et al. (2015)) in angles of inter-regional phase synchronization (Petkoski et al. (2018),  
1112 Petkoski & Jirsa (2019)). However, networks of phase synchronization are physiologically  
1113 distinct from networks of amplitude correlation (Engel et al. (2013)) and exhibit different  
1114 patterns of connectivity (Siems & Siegel (2020)). Similarly, angles of phase synchronization

1115 are distinct from the strengths of phase synchronization that we modelled. In contrast to these  
1116 studies, we demonstrated the role of distance-dependent conduction delays in generating  
1117 alpha-band inter-regional networks of phase synchronization observed in MEG resting-state.

1118

1119 Those few modelling studies which use BNMs with distance-dependent delays to generate  
1120 networks of phase synchronization only contrast them to BNMs with “zero delays”. These  
1121 studies (Abeyesuriya et al. (2018), Finger & Bönstrup et al. (2016)) have demonstrated BNMs  
1122 with distance-dependent delays to generate alpha-band networks of phase synchronization  
1123 more similar to those in MEG or EEG resting-state, than networks from BNMs with “zero  
1124 delays”. However, “zero delays” are biologically implausible, implying infinite conduction  
1125 velocities. In contrast, we demonstrate that BNMs with distance-dependent delays generate  
1126 networks more similar to those in MEG resting-state than those from BNMs implementing  
1127 two biologically plausible methods accounting for spatially varying conduction velocities.

1128

1129 The generation of phenomena observed in MEG, *e.g.*, power spectra, amplitude correlations  
1130 (Cabral et al. (2022), Cabral et al. (2014)) by BNMs with distance-dependent delays has been  
1131 linked to the variability or heterogeneity of these delays (Lee et al. (2009), Touboul (2012)).  
1132 We demonstrate that inter-regional distances rather than delay heterogeneity *per se*, explain  
1133 the similarity between alpha-band networks of phase synchronization generated by BNMs  
1134 with distance-dependent delays, and those observed in MEG resting-state.

1135

1136 Previous neurophysiological and modelling studies have contributed to our understanding of  
1137 the structure-function relationship underlying phase synchronization. For example, studies  
1138 have demonstrated the role of excitatory-inhibitory connections in generating local oscillatory  
1139 dynamics (Buzsáki (2006), Traub et al. (1997)) required for phase synchronization, and the  
1140 role of anatomical connections in promoting inter-regional phase synchronization (Gray  
1141 (1994), Finger & Bönstrup et al. (2016)). In our study, intermediate diagnostics from BOLFI  
1142 model fitting corroborated these previous results. For example, we found supporting evidence  
1143 for the role of intra-regional connections between excitatory and inhibitory populations in  
1144 generating local oscillatory dynamics, and for the role of inter-regional anatomical  
1145 connections in promoting inter-regional phase synchronization. In addition to these previous  
1146 studies, we furnish new understanding on the role of inter-regional delays in generating large-  
1147 scale networks of phase synchronization observed in MEG resting-state. Our results suggest

1148 that the dynamics of brain regions interact through inter-regional anatomical connection via  
1149 distance-dependent delays to generate large-scale networks of phase synchronization.

1150

1151 Inter-regional conduction delays reported in human and animal neurophysiological studies  
1152 provide a basis for comparison to the distance-dependent conduction delays suggested by our  
1153 modelling study. Human studies have reported correlations of 0.44 between tract length and  
1154 the onset latency of the stimulation-based evoked potential in intra-cranial EEG recordings  
1155 (Trebaul et al. (2018)), which is consistent with the linear relationship between inter-regional  
1156 distance and inter-regional delays suggested by our study. Inter-regional delays estimated  
1157 with a model-based approach on intra-cranial EEG recordings (Lemaréchal et al. (2022)) also  
1158 reported a linear relationship between tract length and estimated delays for most brain  
1159 regions, consistent with the distance-dependent delays suggested by our study.

1160

1161 In contrast to the distance-dependent conduction delays reported for most brain regions with  
1162 intra-cranial EEG recordings (Lemaréchal et al. (2022)), some brain regions present highly  
1163 similar conduction delays with several other regions. For example, the right insula has highly  
1164 similar conduction delays between 6–8 ms with several ipsilateral brain regions (Lemaréchal  
1165 et al. (2022)). Animal neurophysiological studies have also presented evidence for  
1166 isochronous delays, in specific brain regions. For example, efferent connections of layer V  
1167 neurons from regions in the rat ventral temporal cortex had largely isochronous conduction  
1168 delays with several ipsilateral brain regions (Chomiak et al. (2008)), and afferent connections  
1169 of layer IV neurons from thalamus also had highly similar delays with a number of cortical  
1170 brain regions (Salami et al. (2003)). These highly similar delays for a few brain regions might  
1171 be due to regulation in conduction velocities by activity-dependent myelination (Noori et al.  
1172 (2020)), in response to specialised roles of these regions in functions involving fine temporal  
1173 coordination, *e.g.*, sensory cue processing (Chomiak et al. (2008), Pajevic et al. (2014)). We  
1174 propose that future work could investigate methods to specify inter-regional delays, which  
1175 account for the region-specific nature of their distance-dependence.

1176

1177 Due to their high delay heterogeneity, BNMs with distance-dependent delays might be prone  
1178 to the dynamical regime of amplitude death, *i.e.*, cessation of oscillations (Atay (2003)).

1179 Phase synchronization cannot occur in regimes of amplitude death due to absence of  
1180 oscillations and in fact, dynamically adjusting conduction velocities by activity-dependent  
1181 myelination regulation has been suggested as a means of avoiding this regime (Pajevic et al.

1182 (2014)). However, our Posterior Predictive Checks revealed oscillatory dynamics from  
1183 several simulations of the fitted BNM with distance-dependent delays, despite the highly  
1184 heterogeneous nature of these delays. Further, BNMs from previous studies (Cabral et al.  
1185 (2022)) report regimes of reduced amplitude rather than amplitude death, despite using  
1186 distance-dependent conduction delays which are highly heterogeneous by nature.

1187

1188 Distance-dependent conduction delays predict long inter-regional delays between spatially  
1189 distant brain regions. These long delays might be deleterious to inter-regional communication  
1190 through phase synchronization, particularly when the lag of phase synchronization is close to  
1191 the oscillatory time period (Aboitiz et al. (2003), Pajevic et al. (2014)). However, modelling  
1192 studies have demonstrated several means by which phase synchronization lags might be  
1193 adjusted, enabling rapid inter-regional communication despite long conduction delays. For  
1194 example, the presence of a common relay region between two interacting regions (Vicente et  
1195 al. (2008)), driving currents (Tiesinga et al. (2010)), or local inhibition (Battaglia et al.  
1196 (2007)) can adjust the lag of phase synchronization towards zero. Hence, temporally precise  
1197 inter-regional communication can occur despite the presence of long inter-regional delays.

1198

1199 We mention some limitations of our study and propose approaches to addressing these. First,  
1200 we used the Euclidean distance between regions divided by conduction velocity to estimate  
1201 inter-regional delays. Using Euclidean distance to specify tract length facilitated comparison  
1202 to several previous modelling studies on brain functional networks (Abey Suriya et al. (2018),  
1203 Hadida et al. (2018), Cabral et al. (2014), Nakagawa et al. (2014), Deco et al. (2009), Ghosh  
1204 et al. (2008)), which also used this measure. However, any spatially varying errors in tract  
1205 length estimation introduced by Euclidean distance could mask the contribution of spatially  
1206 varying conduction velocities in determining inter-regional delays. Diffusion MRI-based  
1207 tractography can potentially provide more accurate estimates of the tract length, but current  
1208 methods are also prone to error from seeding and termination biases (Girard et al. (2014),  
1209 Sotiropoulos & Zalesky (2019)). Future work could employ the ABC workflow we used, to  
1210 compare different methods to specify tract lengths, thereby further constraining BNMs of  
1211 inter-regional networks of phase synchronization. Second, we focused only on alpha-band  
1212 frequencies due to the clear evidence for alpha-band oscillations both in our own MEG  
1213 dataset and in previous MEG resting-state studies (Mahjoory et al. (2020)), oscillations being  
1214 a pre-requisite for phase synchronization. Hence, our findings are only relevant to phase  
1215 synchronization in alpha-band frequencies. However, we note that brain regions also generate

1216 oscillatory activity in delta, low-beta and high-beta frequency bands (Mahjoory et al. (2020)).  
1217 Future modelling work could study phase synchronization in multiple frequency bands by,  
1218 *e.g.*, including multiple generators per brain region (Deco et al. (2017)). Note that broadening  
1219 the range of frequencies studied would change the values of the summary statistics we use to  
1220 describe the BNM dynamics and those in MEG data, likely resulting in changes to the  
1221 posterior distributions of the BNM parameters to those we have reported here. Third, we  
1222 assumed that all brain regions generate oscillations, in line with empirically observed cortex-  
1223 wide alpha-band spectral peaks both in our own MEG dataset and in previous MEG resting-  
1224 state studies (Mahjoory et al. (2020)). However, we acknowledge recent evidence from intra-  
1225 cranial EEG and MEG data suggesting that not all brain regions might generate oscillations  
1226 (Myrov et al. (2023)). Future modelling studies could examine the role of sparse oscillation  
1227 generators across cortex, including the interaction between sparsity and inter-regional delays,  
1228 in the structure-function relationship of large-scale networks of phase synchronization.  
1229 Finally, we assumed BNM parameters governing local dynamics to be identical across brain  
1230 regions. This was effective in limiting the number of BNM parameters to be estimated, while  
1231 introducing region-wise variation in BNM parameters would have exponentially increased  
1232 the volume of parameter space resulting in much higher numbers of BNM simulations  
1233 required to sample the parameters space (Gutmann & Corander (2016)). However, we  
1234 acknowledge empirical evidence for region-wise variation in structural and functional  
1235 properties of brain regions (Markello & Hansen et al. (2022)), and modelling work  
1236 suggesting the utility of informing BNMs with this region-wise variation (Demirtaş et al.  
1237 (2019), Sanz-Perl et al. (2022)) to emulate empirically observed dynamics. Future BNMs of  
1238 inter-regional phase synchronization could parameterise region-wise variation with only a  
1239 few parameters, by, *e.g.*, expressing the variation in terms of empirically observed spatial  
1240 gradients (Mahjoory et al. (2020), Markello & Hansen (2022)).

1241

1242 The ABC workflow that we employed for model fitting and model comparison naturally  
1243 accounted for uncertainty in values of BNM parameters. We also employed a number of  
1244 recommended best practices (Gelman et al. (2020), van de Schoot et al. (2021)) as we  
1245 proceeded from specifying the three BNMs through to fitting these BNMs and comparing the  
1246 fitted BNMs. In particular, we i) used prior distributions of BNM parameters informed by the  
1247 aggregated neurophysiology literature and the literature on modelling brain functional  
1248 networks, ii) verified suitability of the prior distributions and specification of the BNMs with  
1249 Prior Predictive Checks, iii) verified assumptions underlying the BOLFI model fitting with

1250 fake-data simulations, iv) used diagnostics of the GP-based surrogate modelling to assess  
1251 intermediate stages of the BOLFI model fitting, v) employed established convergence  
1252 diagnostics to assess reliability of the estimated posterior distributions of BNM parameters,  
1253 vi) verified that BOLFI fitting had completed without error using Posterior Predictive  
1254 Checks, vii) performed ABC model comparison across a range of discrepancy thresholds, and  
1255 viii) completed a control analysis to rule out alternative explanations for the results of the  
1256 ABC model comparison. We therefore propose that our results are robust. In conclusion, we  
1257 found evidence that distance-dependent delays crucially contribute to the generation of alpha-  
1258 band inter-regional networks of phase synchronization observed in MEG resting-state.  
1259

## 1260 Declarations of Interest

1261 None

## 1262 Acknowledgements

1263 The authors are grateful to the reviewers of this manuscript for their thoughtful comments,  
1264 addressing which has substantively improved the manuscript. Further, we acknowledge  
1265 Finnish Centre for Artificial Intelligence (FCAI), Academy of Finland (NW: 321542, SK:  
1266 292334, 956 319264, MP: 253130, 256472, 281414, 296304, 266745, SP: 266402, 266745,  
1267 303933, 957 325404), Department of Science & Technology (DST), India and Sigrid Juselius  
1268 Foundation, for providing funding for this project. The authors are grateful to Prof. Sitabhra  
1269 Sinha, Dr. Chandrasekhar Kuyyamudi, Dr. Ayush Bharti, Dr. Henri Pesonen, Dr. Michael  
1270 Gutmann and Antti Karvanen for invaluable discussions, and to Alex Aushev, Anirudh Jain,  
1271 Diego Mesquita and Sophie Wharrie for comments on manuscript drafts. Most of all, we are  
1272 very grateful to Jarno Rantaharju, Thomas Pfau, Richard Darst and Enrico Glerean from  
1273 Aalto Scientific Computing, for facilitating use of computational resources provided by the  
1274 Aalto Science-IT project.

## 1275 References

- 1276 1. Abeysuriya R., Hadida J., Sotiropoulos S.N., Jbabdi S., Becker R., Hunt B., Brookes  
1277 M., Woolrich M. (2018) A biophysical model of dynamic balancing of excitation and  
1278 inhibition in fast oscillatory large-scale networks. *PLoS Comput Biol*, 14(2): e1006007



- 1279 2. Aboitiz F., López J., Montiel J. (2003) Long-distance communication in the human  
1280 brain: timing constraints for inter-hemispheric synchrony and the origin of brain  
1281 lateralization. *Biol Res*, 36(1): 89–99
- 1282 3. Aboitiz F., Scheibel A.B., Fisher R.S., Zaidel E. (1992) Fiber composition of the human  
1283 corpus callosum. *Brain Res.*, 598(1–2): 143–153
- 1284 4. Arnold B.J., Gutmann M.U., Grad Y.H., Sheppard S.K., Corander J., Lipsitch M.,  
1285 Hanage W.P. (2018) Weak epistasis may drive adaptation in recombining bacteria.  
1286 *Genetics*, 208(3): 1247–1260
- 1287 5. Asikainen A., Iñiguez G., Ureña-Carrión J., Kaski K., Kivela M. (2020) Cumulative  
1288 effects of triadic closure and homophily in social networks. *Sci. Adv.*, 6(19): eaax7310
- 1289 6. Atay F. (2003) Distributed delays facilitate amplitude death of coupled oscillators. *Phys*  
1290 *Rev Lett.*, 91(9): 094101
- 1291 7. Baillet S. (2017) Magnetoencephalography for brain electrophysiology and imaging.  
1292 *Nat Neurosci.*, 20(3): 327–339
- 1293 8. Battaglia D., Brunel N., Hansel D. (2007) Temporal decorrelation of collective  
1294 oscillations in neural networks with local inhibition and long-range excitation. *Phys*  
1295 *Rev Lett.*, 99: 238106
- 1296 9. Beaumont M.A. (2019) Approximate Bayesian Computation. *Annu. Rev. Stat. Appl.*, 6:  
1297 379–403
- 1298 10. Betancourt M.J., Byrne S., Girolami M. (2014) Optimizing the integrator step size for  
1299 Hamiltonian Monte Carlo. arXiv:1411.6669v2
- 1300 11. Binzegger T., Douglas R., Martin K. (2004) A quantitative map of the circuit of the cat  
1301 primary visual cortex. *J Neurosci*, 24(39): 8441–8453
- 1302 12. Bogacki P., Shampine L. (1996) An efficient Runge-Kutta (4,5) pair. *Comput Math*  
1303 *with Appl*, 32(6): 15–28
- 1304 13. Breakspear M. (2017) Dynamic models of large-scale brain activity. *Nat Neurosci.*  
1305 20(3): 340–352
- 1306 14. Breakspear M., Heitmann S., Daffertshofer A. (2010) Generative models of cortical  
1307 oscillations: neurobiological implications of the Kuramoto model. *Front Hum*  
1308 *Neurosci.*, 4: 190
- 1309 15. Buzsáki (2006) Rhythms of the brain (1st edition). Oxford University Press, USA
- 1310 16. Cabral J., Luckhoo H., Woolrich M., Joensson M., Mohseni H., Baker A., Kringelbach  
1311 M., Deco G. (2014) Exploring mechanisms of spontaneous functional connectivity in

- 1312 MEG: how delayed network interactions lead to structured amplitude envelopes of  
1313 band-pass filtered oscillations. *NeuroImage*, 90: 423–435
- 1314 17. Campagnola L., Seeman S.C., Chartrand T., Kim L., Hoggarth A., Gamlin C., Ito S.,  
1315 Trinh J., Davoudian P., Radaelli C., Kim M.H., Hage T., Braun T., Alfiler L., Andrade  
1316 J., Bohn P., Dalley R., Henry A., Kebede S., Alice M., Sandman D., Williams G.,  
1317 Larsen R., Teeter C., Daigle T.L., Berry K., Dotson N., Enstrom R., Gorham M., Hupp  
1318 M., Dingman L.S., Ngo K., Nicovich P.R., Potekhina L., Ransford S., Gary A., Goldy  
1319 J., McMillen D., Pham T., Tieu M., Siverts L., Walker M., Farrell C., Schroedter M.,  
1320 Slaughterbeck C., Cobb C., Ellenbogen R., Gwinn R.P., Keene C.D., Ko A.L., Ojemann  
1321 J.G., Silbergeld D.L., Carey D., Casper T., Crichton K., Clark M., Dee N., Ellingwood  
1322 L., Gloe J., Kroll M., Sulc J., Tung H., Wadhvani K., Brouner K., Egdorf T., Maxwell  
1323 M., McGraw M., Pom C.A., Ruiz A., Bomben J., Feng D., Hejazinia N., Shi S., Szafer  
1324 A., Wakeman W., Phillips J., Bernard A., Esposito L., D'Orazi F.D., Sunkin S., Smith  
1325 K., Tasic B., Arkhipov A., Sorensen S., Lein E., Koch C., Murphy G., Zeng H., Jarsky  
1326 T. (2022) Local connectivity and synaptic dynamics in mouse and human neocortex.  
1327 *Science*, 375(6585): eabj5861
- 1328 18. Carr C.E., Konishi M. (1990) A circuit for detection of interaural time differences in  
1329 the brain stem of barn owl. *J Neurosci.*, 10(10): 3227–3246
- 1330 19. Chomiak T., Peters S., Hu B. (2008) Functional architecture and spike timing properties  
1331 of corticofugal projections from rat ventral temporal cortex. *J. Neurophysiol.*, 100(1):  
1332 327–335
- 1333 20. Corander J., Fraser C., Gutmann M.U., Arnold B., Hanage W.P., Bentley S.D., Lipsitch  
1334 M., Croucher N.J. (2017) Frequency-dependent selection in vaccine associated  
1335 pneumococcal population dynamics. *Nat Ecol Evol.*, 1(12): 1950–1960
- 1336 21. Cowan J., Neuman J., van Drongelen W. (2016) Wilson-Cowan equations for  
1337 neocortical dynamics. *J Math Neurosci* 6, 1
- 1338 22. da Silva F. (2013) EEG and MEG: Relevance to Neuroscience. *Neuron*, 80(5): 1112–  
1339 1128
- 1340 23. Dale A.M., Liu A.K., Fischl B.R., Buckner R.L., Belliveau J.W., Lewine J.D., Halgren  
1341 E. (2000) Dynamic statistical parametric mapping: combining fMRI and MEG for  
1342 high-resolution imaging of cortical activity. *Neuron*, 26(1): 55–67
- 1343 24. Deco G., Cabral J., Woolrich M.W., Stevner A.B.A., van Hartevelt T.J., Kringelbach  
1344 M.L. (2017) Single or multiple frequency generators in on-going brain activity: A  
1345 mechanistic whole-brain model of empirical MEG data. *NeuroImage*, 152: 538–550

- 1346 25. Deco G., Jirsa V., McIntosh A., Sporns O., Kötter R. (2009) Key role of coupling, delay  
1347 and noise in resting brain fluctuations. *Proc Natl Acad Sci USA*, 106(25): 10302–10307
- 1348 26. Deco G., Jirsa V.K. (2012) Ongoing cortical activity at rest: criticality, multistability  
1349 and ghost attractors. *J Neurosci.*, 32(10): 3366–3375
- 1350 27. Demirtaş M., Burt J.B., Helmer M., Ji J.L., Adkinson B.D., Glasser M.F., Van Essen  
1351 D.C., Sotiropoulos S.N., Anticevic A., Murray J.D. (2019) “Hierarchical Heterogeneity  
1352 across Human Cortex Shapes Large-Scale Neural Dynamics” *Neuron*, 101(6):1181–  
1353 1194
- 1354 28. Destrieux C., Fischl B., Dale A., Halgren E. (2010) Automatic parcellation of human  
1355 cortical gyri and sulci using standard anatomical nomenclature. *NeuroImage*, 53(1): 1–  
1356 15
- 1357 29. Doesburg S.M., Tingling K., MacDonald M.J., Pang E.W. (2017) Development of  
1358 network synchronization predicts language abilities. *J Cogn Neurosci.*, 28(1): 55–68
- 1359 30. Donahue C.J., Sotiropoulos S.N., Jbabdi S., Hernandez-Fernandez M., Behrens T.E.J.,  
1360 Dyrby T.B., Coalson T., Kennedy H., Knoblauch K., van Essen D.C., Glasser M.F.  
1361 (2016) Using diffusion tractography to predict cortical connection strength and  
1362 distance: a quantitative comparison with tracers in the monkey. *J Neurosci.*, 36(25):  
1363 6758–6770
- 1364 31. Dong C., Loy C.C., He K., Tang X. (2015) Image super-resolution using deep  
1365 convolutional networks. *IEEE Trans. Pattern Anal. Mach. Intell.*, 38(2): 295–307
- 1366 32. Donoghue T., Haller M., Peterson E., Varma P., Sebastian P., Gao R., Noto T., Lara  
1367 A.H., Wallis J.D., Knight R.T., Shestyuk A., Voytek B. (2020) Parameterizing neural  
1368 power spectra into periodic and aperiodic components. *Nature Neurosci.*, 23(12): 1655–  
1369 1665
- 1370 33. Dotson N., Goodell B., Salazar R.F., Hoffman S.J., Gray C.M. (2015) Methods, caveats  
1371 and the future of large-scale microelectrode recordings in the non-human primate.  
1372 *Front Syst Neurosci.*, 9: 149
- 1373 34. Dotson N., Salazar R., Gray C. (2014) Frontoparietal correlation dynamics reveal  
1374 interplay between integration and segregation during visual working memory. *J*  
1375 *Neurosci.*, 34(41): 13600–13613
- 1376 35. Douglas R. Martin K., Whitteridge D. (1989) A canonical microcircuit for neocortex.  
1377 *Neural Comput.*, 1(4): 480–488
- 1378 36. Douglas R.J., Martin K.A.C. (2007) Recurrent neuronal circuits in the neocortex. *Curr*  
1379 *Biol.*, 17(13): R496–500

- 1380 37. Engel A.K., Gerloff C., Hilgetag C.C., Nolte G. (2013) Intrinsic coupling modes:  
1381 multiscale interactions in ongoing brain activity. *Neuron*, 80(4): 867–886
- 1382 38. Faisal A., Selen L., Wolpert D. (2008) Noise in the nervous system. *Nat Rev Neurosci*,  
1383 9(4): 292–303
- 1384 39. Finger H.\*, Bönstrup M.\*, Cheng B., Messé A., Hilgetag C., Thomalla G., Gerloff C.,  
1385 König P. (2016) Modeling of large-scale functional brain networks based on structural  
1386 connectivity from DTI: comparison with EEG derived phase coupling networks and  
1387 evaluation of alternative methods along the modeling path. *PLoS Comput Biol*, 12(8):  
1388 e1005025
- 1389 40. Firmin L., Field P., Maier M.A., Kraskov A., Kirkwood P.A., Nakajima K., Lemon  
1390 R.N., Glickstein M. (2014) Axon diameters and conduction velocities in the macaque  
1391 pyramidal tract. *J Neurophysiol*, 112(6): 1229–1240
- 1392 41. Forrester M., Crofts J., Sotiropoulos S.N., Coombes S., O’Dea R. (2020) The role of  
1393 node dynamics in shaping emergent functional connectivity patterns in the brain. *Netw  
1394 Neurosci*, 4(2): 467–483
- 1395 42. Foxe J., Snyder A. (2011) The role of alpha-band brain oscillations as a sensory  
1396 suppression mechanism during selective attention. *Front Psychol.*, 2: 154
- 1397 43. Fries P. (2005) A mechanism for cognitive dynamics: neuronal communication through  
1398 neuronal coherence. *Trends Cogn Sci*, 9(10): 474–480.
- 1399 44. Fries P. (2015) Rhythms for cognition: communication through coherence. *Neuron*,  
1400 88(1): 220–235
- 1401 45. Gelman A., Carlin J.B., Stern H.S., Dunson D.B., Vehtari A., Rubin D.B. (2013)  
1402 Bayesian data analysis (3rd edition), Chapman & Hall/CRC
- 1403 46. Gelman A., Vehtari A., Simpson D., Margossian C.C., Carpenter B., Yao Y., Kennedy  
1404 L., Gabry J., Bürkner P-C., Modrák M. (2020) Bayesian workflow. arXiv preprint  
1405 arXiv:2011.01808
- 1406 47. Geyer C.J. (2011) “Introduction to Markov Chain Monte Carlo.” In *Handbook of  
1407 Markov Chain Monte Carlo*, edited by Steve Brooks, Andrew Gelman, Galin L. Jones,  
1408 and Xiao-Li Meng, 3–48. Chapman; Hall/CRC
- 1409 48. Ghosh A., Rho Y., McIntosh A.R., Kötter R., Jirsa V.K. (2008) Noise during rest  
1410 enables the exploration of the brain’s dynamic repertoire. *PLoS Comput Biol.*, 4(10):  
1411 e1000196
- 1412 49. Girard G., Whittingstall K., Deriche R., Descoteaux M. (2014) Towards quantitative  
1413 connectivity analysis: reducing tractography biases. *NeuroImage*, 98: 266–278

- 1414 50. Gramfort A., Luessi M., Larson E., Engemann D.A., Strohmeier D., Brodbeck C.,  
1415 Parkkonen L., Hämäläinen M.S. (2014) MNE software for processing MEG and EEG  
1416 data. *NeuroImage*, 86: 446–460
- 1417 51. Gray C.M. (1994) Synchronous oscillations in neuronal systems: mechanisms and  
1418 functions. *J Comput Neurosci*. 1(1–2): 11–38
- 1419 52. Green P., Latuszynski K., Pereyra M., Robert C.P. (2015) Bayesian computation: a  
1420 summary of the current state, and samples backwards and forwards. *Stat. Comput.* 25:  
1421 835–862
- 1422 53. Gross J., Schmitz F., Schnitzler I., Kessler K., Shapiro K., Hommel B., Schnitzler A.  
1423 (2004) Modulation of long-range neural synchrony reflects temporal limitations of  
1424 visual attention in humans. *Proc Natl Acad Sci USA*, 101(35): 13050–13055
- 1425 54. Gutmann M.U., Corander J. (2016) Bayesian optimization for likelihood-free inference  
1426 of simulator-based statistical models. *J Mach Learn Res*, 17: 1–47
- 1427 55. Hadida J., Sotiropoulos S.N., Abeysuriya R., Woolrich M., Jbabdi S. (2018) Bayesian  
1428 optimisation of large-scale biophysical networks. *NeuroImage* 174: 219–236
- 1429 56. Haegens S., Cousijn H., Wallis G., Harrison P.J., Nobre A.C. (2014) Inter- and intra-  
1430 individual variability in alpha peak frequency. *NeuroImage*, 92(100): 46–55
- 1431 57. Heitmann S., Auburn M., Breakspear M. (2018) The Brain Dynamics Toolbox for  
1432 MATLAB. *Neurocomputing*, 315: 82–88
- 1433 58. Heitmann S., Rule M., Truccolo W., Ermentrout B. (2017) Optogenetic stimulation  
1434 shifts the excitability of cerebral cortex from type I to type II: oscillation onset and  
1435 wave propagation. *PLoS Comput Biol* 13(1): e1005349
- 1436 59. Hellyer P., Jachs B., Clopath C., Leech R. (2016) Local inhibitory plasticity tunes  
1437 macroscopic brain dynamics and allows the emergence of functional brain networks.  
1438 *NeuroImage*, 124(Part A): 85–95
- 1439 60. Hirvonen J., Monto S., Wang S., Palva J.M., Palva S. (2018) Dynamic large-scale  
1440 network synchronization from perception to action. *Netw Neurosci*, 2(4): 442–463
- 1441 61. Hlinka J., Coombes S. (2012) Using computational models to relate structural and  
1442 functional brain connectivity. *Eur J Neurosci*, 36(2): 2137–2145
- 1443 62. Hoffman M.D., Gelman A. (2014) The No-U-Turn sampler: adaptively setting path  
1444 lengths in Hamiltonian Monte Carlo. *J. Mach. Learn. Res.* 15(1): 1593–1623
- 1445 63. Jansen B., Rit V. (1995) Electroencephalogram and visual evoked potential generation  
1446 in a mathematical model of coupled cortical columns. *Biol Cybern*, 73: 357–366

- 1447 64. Kandel E.R., Schwartz J.H. (1985) Principles of neural science (2nd edition). McGraw-  
1448 Hill.
- 1449 65. Kangasrääsio A., Jokinen J.P.P., Oulasvirta A., Howes A., Kaski S. (2019) Parameter  
1450 inference for computational cognitive models with Approximate Bayesian  
1451 Computation. *Cognitive Science*, 43(6): e12738
- 1452 66. Kilpatrick Z. (2013) Wilson-Cowan model. *In: Encyclopedia of Computational*  
1453 *Neuroscience*, edited by Jaeger D., Jung R. New York: Springer, 1–5
- 1454 67. Kitzbichler M., Henson R., Smith M., Nathan P., Bullmore E. (2011) Cognitive effort  
1455 drives workspace configuration of human brain functional networks. *J Neurosci*,  
1456 31(22): 8259–8270
- 1457 68. Klimesch W. (2012)  $\alpha$ -band oscillations, attention, and controlled access to stored  
1458 information. *Trends Cogn Sci.*, 16(12): 606-617
- 1459 69. Korhonen O., Palva S., Palva J.M. (2014) Sparse weightings for collapsing inverse  
1460 solutions to cortical parcellations optimize M/EEG source reconstruction accuracy. *J*  
1461 *Neurosci Methods*, 226, 147–160
- 1462 70. Kuramoto Y. (1984) Chemical Oscillations, Waves and Turbulence. *Mineola, NY:*  
1463 *Dover Publications*.
- 1464 71. Leclercq F. (2018) Bayesian optimization for likelihood-free cosmological inference.  
1465 *Phys. Rev. D*, 98: 063511
- 1466 72. Ledig C., Theis L., Huszar F., Caballero J., Cunningham A., Acosta A., Aitken A.,  
1467 Tejani A., Totz J., Wang Z., Shi W. (2017) Photo-realistic single image super-resolution  
1468 using a generative adversarial network. *Proc. IEEE Comput. Soc. Conf. Vis. Pattern*  
1469 *Recognit.*, 4681–4690
- 1470 73. Lee S.W., Ott E., Antonsen T.M. (2009) Large coupled oscillator systems with  
1471 heterogeneous interaction delays. *Phys. Rev. Lett.*, 103: 044101
- 1472 74. Lemaréchal J.D., Jedynek M., Trebaul L., Boyer A., Tadel F., Bhattacharjee M., Deman  
1473 P., Tuyisenge V., Ayoubian L., Hugues E., Chanteloup-Forêt B., Saubat C., Zouglech  
1474 R., Reyes Mejia G.C., Tourbier S., Hagmann P., Adam C., Barba C., Bartolomei F.,  
1475 Blauwblomme T., Curot J., Dubeau F., Francione S., Garcés M., Hirsch E., Landré E.,  
1476 Liu S., Maillard L., Metsähonkala E.L., Mindruta I., Nica A., Pail M., Petrescu A.M.,  
1477 Rheims S., Rocamora R., Schulze-Bonhage A., Szurhaj W., Taussig D., Valentin A.,  
1478 Wang H., Kahane P., George N., David O.; F-TRACT consortium. (2022) A brain atlas  
1479 of axonal and synaptic delays based on modelling of cortico-cortical evoked potentials.  
1480 *Brain*, 145(5):1653–1667

- 1481 75. Lintusaari J., Gutmann M., Dutta R., Kaski S., Corander J. (2017) Fundamentals and  
1482 recent developments in Approximate Bayesian Computation. *Syst Biol*, 66(1): e66-e82
- 1483 76. Lintusaari J., Vuollekoski H., Kangasrääsio A., Skytén K., Järvenpää M., Marttinen P.,  
1484 Gutmann M., Vehtari A., Coriander J., Kaski S. (2018) ELFI: Engine for Likelihood-  
1485 Free Inference. *J Mach Learn Res*, 19(16): 1–7
- 1486 77. Lobier M., Palva J.M., Palva S. (2018) High-alpha band synchronization across frontal,  
1487 parietal and visual cortex mediates behavioural and neuronal effects of visuospatial  
1488 attention. *NeuroImage*, 165: 222–237
- 1489 78. Mahjoory K., Schoffelen J-M., Keitel A., Gross J. (2020) The frequency gradient of  
1490 human resting-state brain oscillations follows cortical hierarchies. *eLife*, 9: e53715
- 1491 79. Markello R.D.\*, Hansen J.Y.\*, Liu Z.Q., Bazinet V., Shafiei G., Suárez L.E., Blostein  
1492 N., Seidlitz J., Baillet S., Satterthwaite T.D., Chakravarty M.M., Raznahan A., Mischak  
1493 B. neuromaps: structural and functional interpretation of brain maps. *Nat Methods*,  
1494 19(11): 1472–1479
- 1495 80. Markram H., Toledo-Rodriquez M., Wang Y., Gupta A., Silberberg G., Wu C. (2004)  
1496 Interneurons of the neocortical inhibitory system. *Nat Rev Neurosci.*, 5(10): 793–807
- 1497 81. McNally A.\*, Kallonen T.\*, Conner C., Abudahab K., Aanensen D.M., Horner C.,  
1498 Peacock S.J., Parkhill J., Croucher N.J., Corander J. (2019) Diversification of  
1499 colonization factors in a multidrug-resistant escherichia coli lineage evolving under  
1500 negative frequency-dependent selection. *mBio*, 10(2): e00644–19
- 1501 82. Meijas J.F., Murray J.D., Kennedy H., Wang X-J. (2016) Feedforward and feedback  
1502 frequency-dependent interactions in a large-scale laminar network of the primate  
1503 cortex. *Sci. Adv.*, 2: e1601335
- 1504 83. Miller R. (1975) Distribution and properties of commissural and other neurons in cat  
1505 sensorimotor cortex. *J. Comp. Neurol.*, 164(3): 361–373
- 1506 84. Mostame P., Sadaghiani S. (2021) Oscillation-based connectivity architecture is  
1507 dominated by an intrinsic spatial organization, not cognitive state or frequency. *J*  
1508 *Neurosci.*, 41(1):179-192
- 1509 85. Myrov V., Siebenhühner F., Juvonen J.J., Arnulfo G., Palva S., Matias J.M. (2023)  
1510 Discovering rhythmicity of neuronal oscillations. *Research Square*
- 1511 86. Nakagawa T., Woolrich M., Luckhoo H., Joensson M, Mohseni H., Kringelbach M.,  
1512 Jirsa V., Deco G. (2014) How delays matter in an oscillatory whole-brain spiking-  
1513 neuron network model for MEG alpha-rhythms at rest. *NeuroImage*, 87: 383–394.

- 1514 87. Nentwich M., Ai L., Madsen J., Telesford Q.K., Haufe S., Milham M.P., Parra L.C.  
1515 (2020) Functional connectivity of EEG is subject-specific, associated with phenotype,  
1516 and different from fMRI. *NeuroImage*, 218:117001
- 1517 88. Noori R., Park D., Griffiths J., Bells S., Frankland P., Mabbott D., Lefebvre J. (2020)  
1518 Activity-dependent myelination: a glial mechanism of oscillatory self-organization in  
1519 large-scale brain networks. *Proc Natl Acad Sci USA*, 117(24): 13227–13237
- 1520 89. Oostenveld R., Fries P., Maris E., Schoffelen J-M. (2011) FieldTrip: Open source  
1521 software for advanced analysis of MEG, EEG and invasive electrophysiological data.  
1522 *Comput Intell Neurosci* 2011(1): 156869
- 1523 90. Pajevic S., Basset P.J., Fields R.D. (2014) Role of myelin plasticity in oscillations and  
1524 synchrony of neuronal activity. *Neuroscience*, 276: 135–147
- 1525 91. Palva J.M., Monto S., Kulashekhar S., Palva S. (2010) Neuronal synchrony reveals  
1526 working memory networks and predicts individual memory capacity. *Proc Natl Acad  
1527 Sci USA*, 107(16): 7580–7585
- 1528 92. Palva J.M., Wang S.H., Palva S., Zhigalov A., Monto S., Brookes M., Schoffelen J-M.,  
1529 Jerbi K. (2018) Ghost interactions in MEG/EEG source space: a note of caution on  
1530 inter-areal coupling measures. *NeuroImage*, 173: 632–643
- 1531 93. Palva S., Palva J.M. (2007) New vistas for alpha-frequency band oscillations. *Trends  
1532 Neurosci.*, 30(4): 150–158
- 1533 94. Perl Y.S., Bocaccio H., Pérez-Ipiña I., Zamberlán F., Piccinini J., Laufs H., Kringelbach  
1534 M., Deco G., Tagliazucchi E. (2020) Generative embeddings of brain collective  
1535 dynamics using variational autoencoders. *Phys. Rev. Lett.*, 125: 238101
- 1536 95. Perl, Y. S., Zamora-Lopez, G., Montbrió, E., Monge-Asensio, M., Vohryzek, J.,  
1537 Fittipaldi, S., Campo, C. G., Moguilner, S., Ibañez, A., Tagliazucchi, E., Yeo, B. T. T.,  
1538 Kringelbach, M. L. & Deco, G. (2022). The impact of regional heterogeneity in whole-  
1539 brain dynamics in the presence of oscillations. *Netw. Neurosci.*, 1–42
- 1540 96. Petkoski S., Jirsa V.K. (2019) Transmission time delays organise the brain network  
1541 synchronization. *Phil Trans A Math Phys Eng Sci.*, 377(2153): 20180132
- 1542 97. Petkoski S., Palva J.M., Jirsa V.K. (2018) Phase-lags in large scale brain  
1543 synchronization: methodological considerations and in-silico analysis. *PLoS Comput  
1544 Biol.*, 14(7): e1006160
- 1545 98. Piccinini J., Pérez-Ipiña I., Laufs H., Kringelbach M., Deco G., Perl Y.S., Tagliazucchi  
1546 E. (2021) Noise-driven multistability vs deterministic chaos in phenomenological semi-  
1547 empirical models of whole-brain activity. *Chaos*, 31(2): 023127



- 1548 99. Rasmussen C.E., Williams C.K.I. (2006) Gaussian Processes for Machine Learning,  
1549 MIT Press
- 1550 100. Rushton W.A.H. (1951) A theory of the effects of fibre size in medullated nerve.  
1551 *J. Physiol.* 115(1): 101–122
- 1552 101. Sadaghiani S., Brookes M.J., Baillet S. (2022) Connectomics of human  
1553 electrophysiology. *NeuroImage*, 247:118788.
- 1554 102. Salami M., Itami C., Tsumoto T., Kimura F. (2003) Change of conduction  
1555 velocity by regional myelination yields constant latency irrespective of distance  
1556 between thalamus and cortex. *Proc Natl Acad Sci USA*, 100(10): 6174–6179
- 1557 103. Salazar R.F., Dotson N.M., Bressler S.L., Gray C.M. (2012) Content-specific  
1558 fronto-parietal synchronization during visual working memory. *Science*, 338(6110):  
1559 1097–1100
- 1560 104. Seeman S.C.\*, Campagnola L.\*, Davoudian P.A., Hoggarth A., Hage T.A.,  
1561 Bosma-Moody A., Baker C.A., Lee J.H., Mihalas S., Teeter C., Ko A.L., Ojemann J.G.,  
1562 Gwinn R.P., Silbergeld D.L., Cobbs C., Phillips J., Lein E., Murphy G., Koch C., Zeng  
1563 H., Jarsky T. (2018) Sparse recurrent excitatory connectivity in the microcircuit of the  
1564 adult mouse and human cortex. *Elife*, 7: e37349
- 1565 105. Seidl A. (2014) Regulation of conduction time along axons. *Neuroscience*, 276:  
1566 126–134
- 1567 106. Shampine L., Thompson S. (2001) Solving DDEs in MATLAB. *Appl Numer*  
1568 *Math*, 37(4): 441–458
- 1569 107. Siebenhühner F., Lobier M., Wang S.H., Palva S., Palva J.M. (2016) Measuring  
1570 large-scale synchronization with human MEG and EEG: challenges and solutions.  
1571 *Multimodal oscillation-based connectivity theory*, Springer International Publishing, 1–  
1572 18
- 1573 108. Siebenhühner F., Wang S., Arnulfo G., Lampinen A., Nobili L., Palva J.M.,  
1574 Palva S. (2020) Genuine cross-frequency coupling networks in human resting-state  
1575 electrophysiological recordings. *PLoS Biol*, 18(5): e3000685
- 1576 109. Siems M., Siegel M. (2020) Dissociated neuronal phase- and amplitude-  
1577 coupling patterns in the human brain. *NeuroImage*, 209:116538
- 1578 110. Simmons P.A., Pearlman A.L. (1983) Receptive-field properties of transcallosal  
1579 visual cortical neurons in the normal and reeler mouse. *J. Neurophysiol.*, 50(4): 838–  
1580 848

- 1581 111. Sisson S.A., Fan Y., Tanaka M.M. (2007) Sequential Monte Carlo without  
1582 likelihoods. *Proc Natl Acad Sci USA*, 104(6): 1760–1765
- 1583 112. Smith R., Tournier J., Calamante F., Connelly A. (2012) Anatomically-  
1584 constrained tractography: improved diffusion MRI streamlines tractography through  
1585 effective use of anatomical information. *NeuroImage*, 62(3): 1924–1938
- 1586 113. Smith R., Tournier J., Calamante F., Connelly A. (2013) SIFT: Spherical-  
1587 deconvolution informed filtering of tractograms. *NeuroImage*, 67: 298–312
- 1588 114. Sotiropoulos S.N., Zalesky A. (2019) Building connectomes using diffusion  
1589 MRI: why, how and but. *NMR Biomed.* 32(4): e3752
- 1590 115. Sunnåker M., Busetto A.G., Numminen E., Corander J., Foll M., Dessimoz C.  
1591 (2013) Approximate Bayesian Computation. *PLoS Comput Biol*, 9(1): e1002803
- 1592 116. Swadlow H.A. (1990) Efferent neurons and suspected interneurons in S-1  
1593 forepaw representation of the awake rabbit: receptive fields and axonal properties. *J.*  
1594 *Neurophysiol.*, 63(6): 1477–1498
- 1595 117. Swadlow H.A., Rosene D.L., Waxman S.G. (1978) Characteristics of  
1596 interhemispheric impulse conduction between prelunate gyri of the rhesus monkey.  
1597 *Exp. Brain Res.*, 33(3–4):455–467
- 1598 118. Taulu S., Hari R. (2009) Removal of magnetoencephalographic artifacts with  
1599 temporal signal-space separation: demonstration with single-trial auditory-evoked  
1600 responses. *Hum Brain Mapp*, 30: 1524–1534
- 1601 119. Tiesinga P., Sejnowski T. (2010) Mechanisms for phase shifting in cortical  
1602 networks and their role in communication through coherence. *Front Hum Neurosci*, 4,  
1603 196
- 1604 120. Touboul J. (2012) Limits and dynamics of stochastic neuronal networks with  
1605 random heterogeneous delays. *J. Stat. Phys.*, 149: 569–597
- 1606 121. Traub R., Jefferys J., Whittington M. (1997) Simulation of gamma rhythms in  
1607 networks of interneurons and pyramidal cells. *J Comput Neurosci* 4(2): 141–150
- 1608 122. Trebault L., Deman P., Tuyisenge V., Jedynak M., Hugues E., Rudrauf D.,  
1609 Bhattacharjee M., Tadel F., Chanteloup-Foret B., Saubat C., Reyes Mejia G.C., Adam  
1610 C., Nica A., Pail M., Dubeau F., Rheims S., Trébouchon A., Wang H., Liu S.,  
1611 Blauwblomme T., Garcés M., De Palma L., Valentin A., Metsähonkala E.L., Petrescu  
1612 A.M., Landré E., Szurhaj W., Hirsch E., Valton L., Rocamora R., Schulze-Bonhage A.,  
1613 Mindruta I., Francione S., Maillard L., Taussig D., Kahane P., David O. (2018)

- 1614 Probabilistic functional tractography of the human cortex revisited. *NeuroImage*,  
1615 181:414–429
- 1616 123. Tripathy S., Burton S., Geramita M., Gherkin R.C., Urban N.N. (2015) Brain-  
1617 wide analysis of electrophysiological diversity yields novel categorization of  
1618 mammalian neuron types. *J Neurophysiol.* 113(10): 3474–3489
- 1619 124. Tripathy S., Savitskaya J., Burton S., Urban N.N., Gherkin R.C. (2014)  
1620 NeuroElectro: a window to the world’s neuron electrophysiology data. *Front*  
1621 *Neuroinform.*, 8: 40
- 1622 125. van de Schoot R., Depaoli S., King R., Kramer B., Märtens K., Tadesse M.G.,  
1623 Vannucci M., Gelman A., Veen D., Willemsen J., Yau C. (2021) Bayesian statistics and  
1624 modelling. *Nat Rev Methods Primers*, 1(1): 1-26
- 1625 126. van Essen D.C., Smith S.M., Barch D.M., Behrens T.E.J., Yacoub E., Ugurbil  
1626 K., WU-Minn HCP Consortium (2013) The WU-Minn Human Connectome Project: an  
1627 overview. *NeuroImage*, 80: 62–79
- 1628 127. Varela F., Lachaux J-P., Rodriguez E., Martinerie J. (2001). The brainweb:  
1629 phase synchronization and large-scale integration. *Nat Rev Neurosci.* 2(4): 229–239
- 1630 128. Vehtari A., Gelman A., Simpson D., Carpenter B., Bürkner P.C. (2021) Rank-  
1631 normalization, folding and localization: an improved  $\hat{R}$  for assessing convergence of  
1632 MCMC. *Bayesian Anal.*, 16(2): 667–718
- 1633 129. Vicente R., Gollo L., Mirasso C.R., Fischer I., Pipa G. (2008) Dynamical  
1634 relaying can yield zero time lag neuronal synchrony despite long conduction delays.  
1635 *Proc Natl Acad Sci USA*, 105(44): 17157–17162
- 1636 130. Vidaurre D., Hunt L.T., Quinn A.J., Hunt B.A.E., Brookes M.J., Nobre A.C.,  
1637 Woolrich M.W. (2018) Spontaneous cortical activity transiently organises into  
1638 frequency specific phase-coupling networks. *Nat Commun*, 9(1): 2987.
- 1639 131. Vinck M., Oostenveld R., Wingerden M., Battaglia F., Pennartz C. (2011) An  
1640 improved index of phase-synchronization for electrophysiological data in the presence  
1641 of volume-conduction, noise and sample-size bias. *NeuroImage*, 55(4): 1548–1565
- 1642 132. Wang X-J. (2010) Neurophysiological and computational principles of cortical  
1643 rhythms in cognition. *Physiol Rev*, 90(3): 1195–1268
- 1644 133. Wang Y., Gupta A., Toledo-Rodriguez M., Wu C.Z., Markram H. (2002)  
1645 Anatomical, physiological, molecular and circuit properties of nest basket cells in the  
1646 developing somatosensory cortex. *Cereb Cortex.*, 12(4): 395–410

- 1647 134. Wang Z., Bovik A.C., Sheikh H.R., Simoncelli E.P. (2004) Image quality  
1648 assessment: from error visibility to structural similarity. *IEEE Trans Image Process.*,  
1649 13(4): 600–612
- 1650 135. Wang Z., Lu L., Bovik A.C. (2004a) Video quality assessment based on  
1651 structural distortion measurement. *Signal Process. Image Commun.*, 19(2): 121–132
- 1652 136. Waxman S.G., Bennett M.V.L. (1972) Relative conduction velocities of small  
1653 myelinated and non-myelinated fibres in the central nervous system. *Nature New Biol.*  
1654 238(85): 217–219
- 1655 137. West T.O., Berthouze L., Farmer S.F., Cagnan H., Litvak V. (2021) Inference  
1656 of brain networks with approximate Bayesian computation - assessing face validity with  
1657 an example application in Parkinsonism. *NeuroImage*, 236: 118020
- 1658 138. Williams, N., Ojanperä, A., Siebenhühner, F., Toselli, B., Palva, S., Arnulfo,  
1659 G., Kaski, S.; Palva, M. (2023), “Biological constraints for parameter values of large-  
1660 scale biologically plausible human Neuroscience models”, Mendeley Data, V1, doi:  
1661 10.17632/5kgw7ssbpx.1
- 1662 139. Wilson H., Cowan J. (1972) Excitatory and inhibitory interactions in localized  
1663 populations of model neurons. *Biophys J*, 12(1): 1–24
- 1664 140. Womelsdorf T., Schoffelen J.M., Oostenveld R., Singer W., Desimone R.,  
1665 Engel A., Fries P. (2007) Modulation of neuronal interactions through neuronal  
1666 synchronization. *Science*, 316(5831): 1609–1612
- 1667 141. Woolrich M., Stephan K. (2013) Biophysical network models and the human  
1668 connectome. *NeuroImage*, 80: 330–338
- 1669 142. Xia M., Wang J., He Y. (2013) BrainNet Viewer: A Network Visualization Tool  
1670 for Human Brain Connectomics. *PLoS ONE* 8: e68910

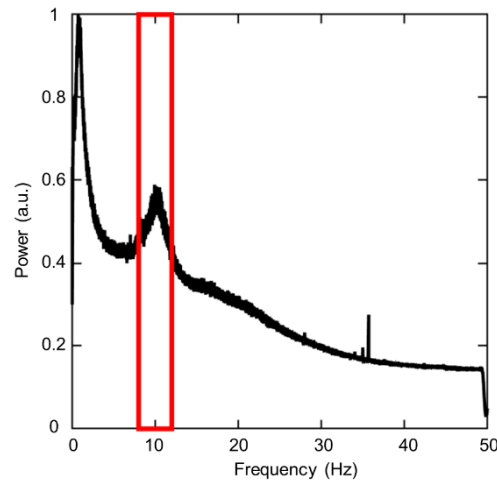
1671

1672

1673

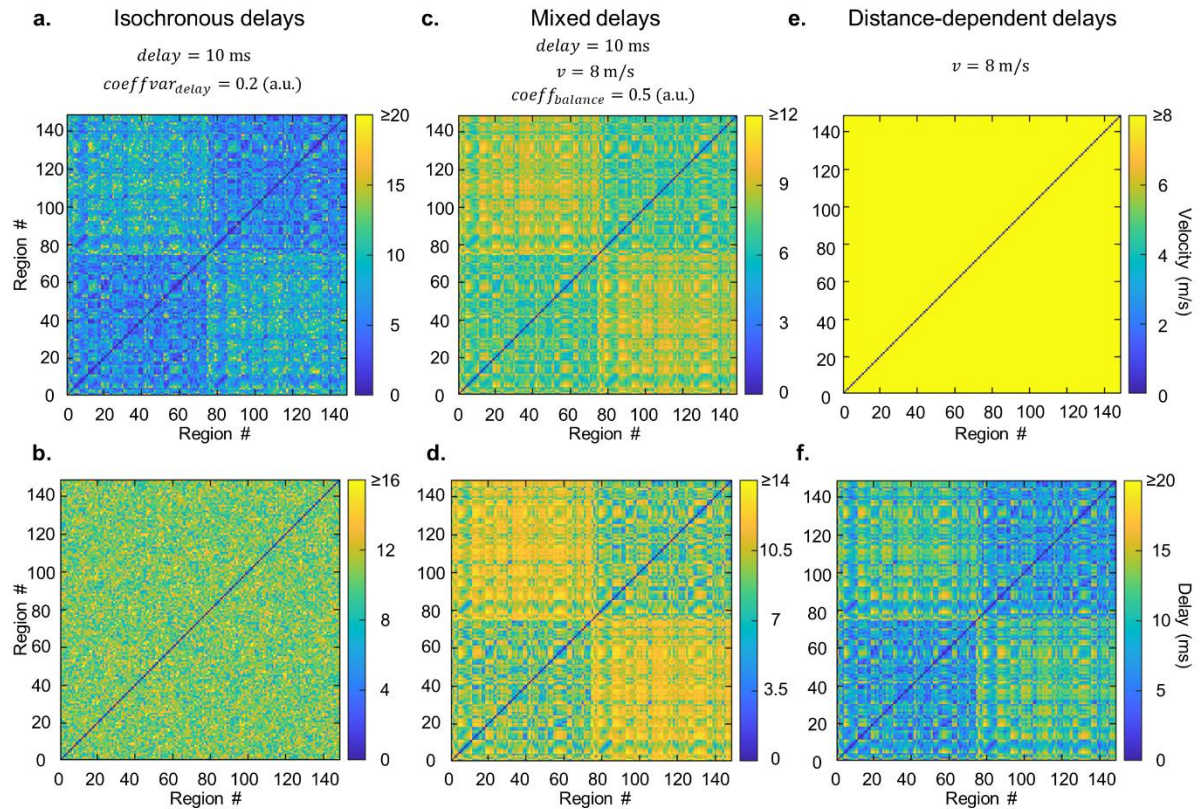
1674

1675 **Supplementary figures**



1676 **Figure S1. Group-level frequency spectrum displays alpha-band spectral peak.** Group-  
1677 level frequency spectrum averaged across brain regions, of source-reconstructed MEG  
1678 resting-state data. Red borders of rectangle outline band of alpha frequencies (8–12 Hz).

1680  
1681  
1682  
1683  
1684  
1685  
1686  
1687  
1688



1689

1690

1691 **Figure S2. Specifying inter-regional delays for “isochronous delays”, “mixed delays”**

1692 **and “distance-dependent delays” methods. a-b.** Matrices of inter-regional conduction

1693 velocities and conduction delays for “isochronous delays” method, **c-d.** Matrices of inter-

1694 regional conduction velocities and conduction delays for “mixed delays” method, **e-f.**

1695 Matrices of inter-regional conduction velocities and conduction delays for “distance-

1696 dependent delays” method.

1697

1698

1699

1700

1701

1702

1703

1704

1705

1706

1707

1708

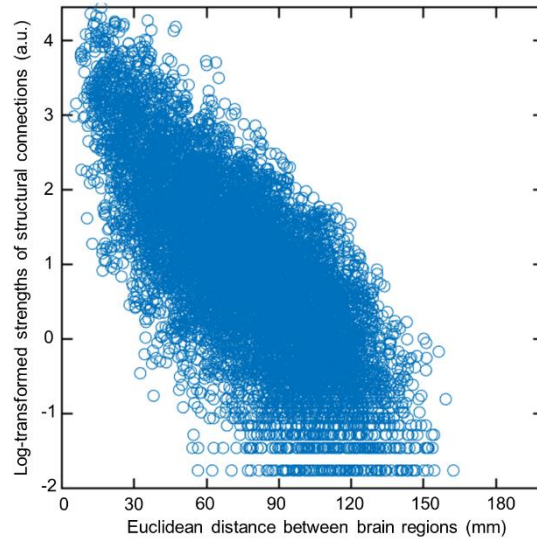
1709

1710

1711

1712

1713



1714

1715

**Figure S3. Log-transformed strengths of structural connections are inversely related to**

1716

**distance between brain regions.** Scatter plot of Euclidean distance between every pair of

1717

brain regions in the 148-region Destrieux brain atlas and log-transformed strengths of

1718

structural connections between these regions.

1719

1720

1721

1722

1723

1724

1725

1726

1727

1728

1729

1730

1731

1732

1733

1734

1735

1736

1737

1738

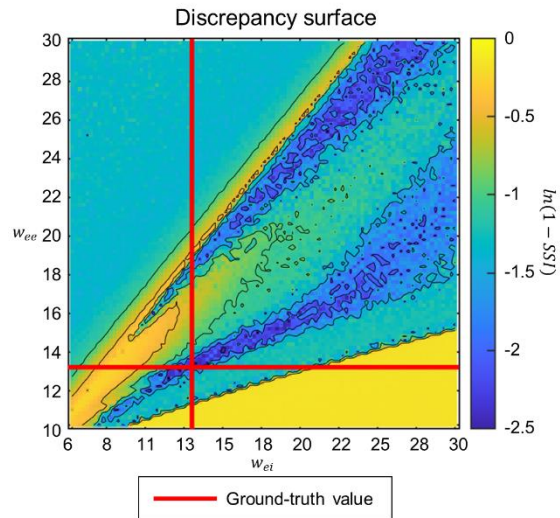
1739

1740

1741

1742

1743



1744

1745 **Figure S4. Gaussian Process (GP)-predicted discrepancies are sensitive to values of**

1746 **BNM parameters**  $100 \times 100$  grid of GP-predicted discrepancies between summary statistics

1747 of BNM dynamics at every pair of  $w_{ee}$  and  $w_{ei}$  values, and BNM dynamics at  $w_{ee}=12.9$ ,

1748  $w_{ei}=13.4$ .  $w_{ee}$  is the strength of connections within excitatory neuronal populations,  $w_{ei}$  is the

1749 strength of connections from inhibitory to excitatory neuronal populations. Red lines indicate

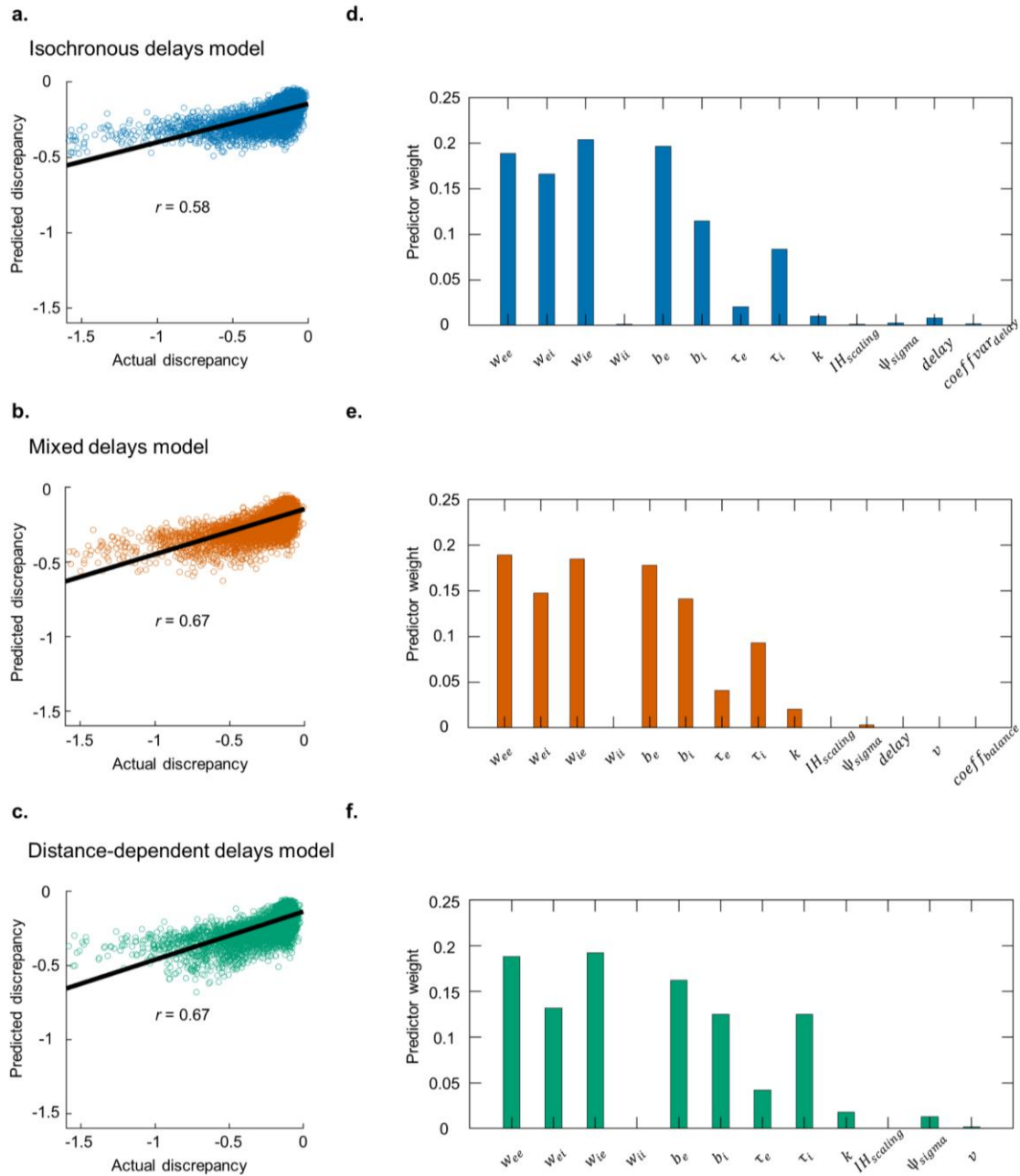
1750 ground-truth values of  $w_{ee}$  and  $w_{ei}$ . Discrepancies were measured by  $\ln(1 - SSI)$ . SSI is the

1751 Structural Similarity Index.

1752

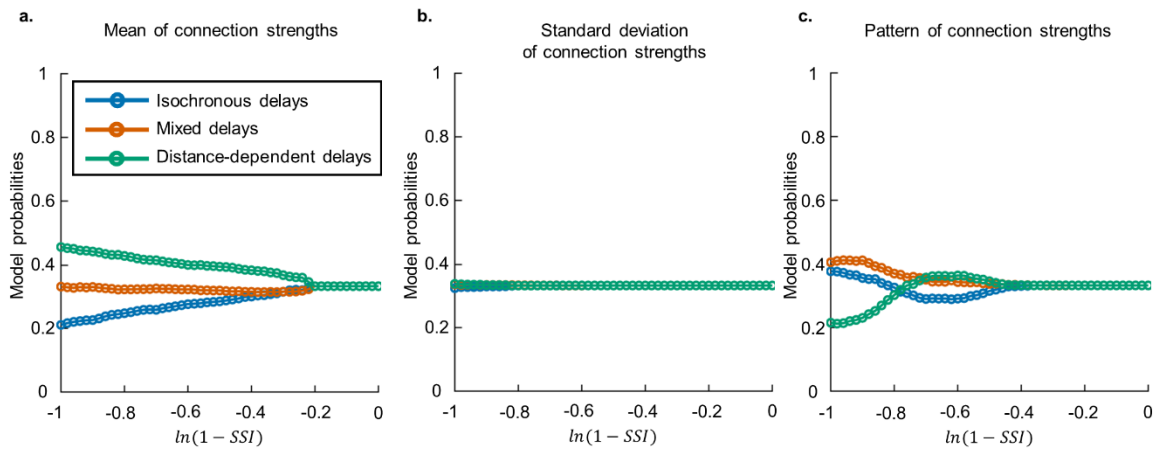
1753





1754  
1755  
1756  
1757  
1758  
1759  
1760  
1761  
1762  
1763

**Figure S5. Gaussian Process (GP) regression results during application of BOLFI to fit BNMs to MEG resting-state data. a-c** Scatter plot of actual and GP-predicted discrepancies between BNM dynamics and MEG data, for the “isochronous delays”, “mixed delays” and “distance-dependent delays” methods respectively. **d-f** Relative importance of each BNM parameter in predicting discrepancies BNM dynamics and MEG data, for the three methods.



1764

1765 **Figure S6. BNM with “distance-dependent delays” most probable when comparing**  
1766 **mean of connection strengths, but not their standard deviation or pattern. a.** Model  
1767 probabilities of BNMs with “isochronous delays”, “mixed delays” and “distance-dependent  
1768 delays”, when comparing mean of connection strengths. **b.** Model probabilities of BNMs  
1769 with “isochronous delays”, “mixed delays” and “distance-dependent delays”, when  
1770 comparing standard deviation of connection strengths. **c.** Model probabilities of BNMs with  
1771 “isochronous delays”, “mixed delays” and “distance-dependent delays”, when comparing  
1772 pattern of connection strengths. Discrepancies are estimated as  $\ln(1 - SSI)$ , where SSI is the  
1773 Structural Similarity Index.

1774

1775

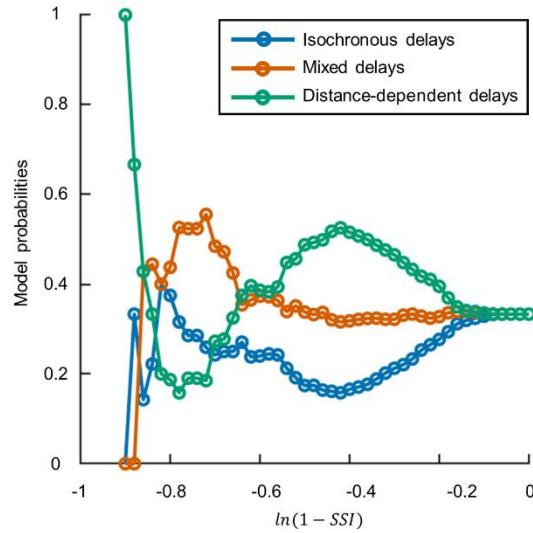
1776

1777

1778

1779

1780



1781

1782 **Figure S7. BNM with “distance-dependent delays” more probable than BNMs with**  
1783 **“isochronous delays” and “mixed delays” for eyes-closed MEG resting-state data.** Model  
1784 probabilities of BNMs with “isochronous delays”, “mixed delays”, and “distance-dependent  
1785 delays”, for a range of minimum discrepancies between phase synchronization strengths of  
1786 BNM dynamics and MEG eyes-closed resting-state data. Discrepancies are estimated as  
1787  $\ln(1 - SSI)$ , where SSI is the Structural Similarity Index.

1788

1789

1790

1791

1792

1793

1794

1795

1796

1797

1798

1799

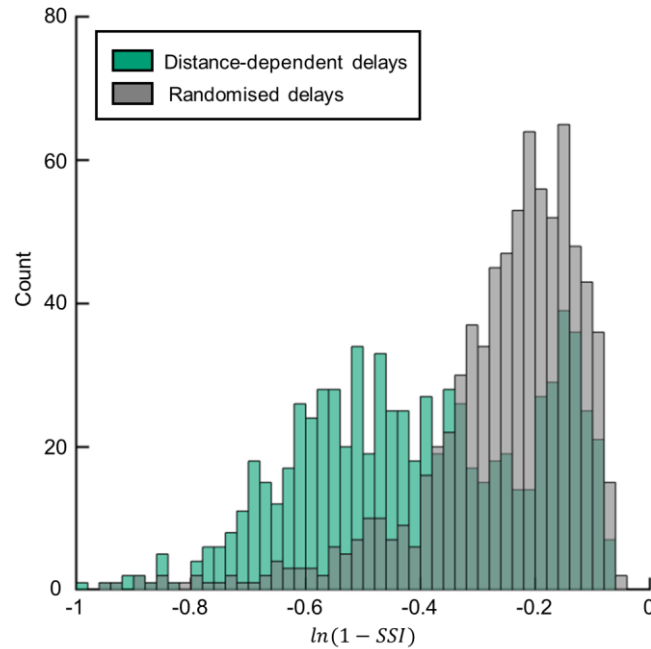
1800

1801

1802

1803

1804



1805

1806 **Figure S8. Delay heterogeneity does not explain correspondence between phase**  
1807 **synchronization strengths of dynamics from BNM with “distance-dependent delays”**  
1808 **and those in MEG data.** Histogram of discrepancies between dynamics of BNM with  
1809 “distance-dependent delays” (green) and MEG data, and histogram of discrepancies between  
1810 dynamics of BNM with “randomised delays” (gray) and MEG data. Histogram overlap is also  
1811 shown (dark green). Discrepancies are  $\ln(1 - SSI)$ , SSI is the Structural Similarity Index.

1812